

1 **Glacial-interglacial shifts in dominant climate forcing over the last 33** 2 **ka in the northern South China Sea**

3 Xueqin Zhao^{*1}, Shengjie Ye¹, Jiahui Yao¹, Michael E. Meadows^{2,3}, Chengyu Weng⁴, Yasong Wang¹,
4 Mingxing Zhang¹, Yunping Xu¹

5 ¹Shanghai Frontiers Research Center of the Hadal Biosphere, College of Oceanography and Ecological Science, Shanghai
6 Ocean University, Shanghai 201306, China

7 ²School of Geography and Ocean Sciences, Nanjing University, Nanjing 210023, China

8 ³Department of Environmental & Geographical Science, University of Cape Town, Cape Town 7701, South Africa

9 ⁴State Key Laboratory of Marine Geology, Tongji University, Shanghai, China

10 *Correspondence to:* Xueqin Zhao (xqzhao@shou.edu.cn)

11 **Abstract.** The northern South China Sea (SCS) is a critical region for understanding East Asian Monsoon dynamics. However,
12 integrated, multi-proxy records elucidating long-term climatic and vegetation changes in this region remain fragmented, with
13 a notable scarcity of coherent land-ocean interaction data during the Last Glacial Maximum (LGM). This gap has impeded
14 progress in elucidating the mechanisms underpinning monsoon variability and in rigorously evaluating the performance of
15 palaeoclimate models. To address this, we conducted a multi-proxy analysis combining palynological, organic- and inorganic-
16 geochemical methods on a marine sediment core from the northern SCS to reconstruct environmental and oceanic dynamics
17 at millennial-scale resolution that spans the last 33 ka. Our results reveal a clear contrast between glacial and interglacial
18 regimes. The glacial period, especially the LGM, was characterized by higher sedimentation rates, elevated marine primary
19 productivity, cooler and drier conditions, herb-dominated vegetation, and intensified fire activity. This regime was dominantly
20 forced by low sea level and glacial aridity, which together promoted open terrestrial vegetation and enhanced nutrient input to
21 the ocean. The deglaciation was characterized by pronounced warming, reduced productivity, increased moisture availability,
22 a shift to pine-dominated vegetation, and reduced fire activity. A key finding is the ocean warming which began around 1.3 ka
23 earlier than major terrestrial changes, indicating that tropical ocean-atmosphere interactions initiated the deglacial transition.
24 The overall findings highlight a fundamental transition in climatic controls, from a glacial regime dominated by sea-level-
25 driven shelf exposure and arid climate to an interglacial regime governed by tropical ocean-atmosphere dynamics. This study
26 underscores the sensitivity of the northern SCS to both high- and low-latitude forcing and the value of integrated land-sea
27 proxies in deciphering complex climate interactions.

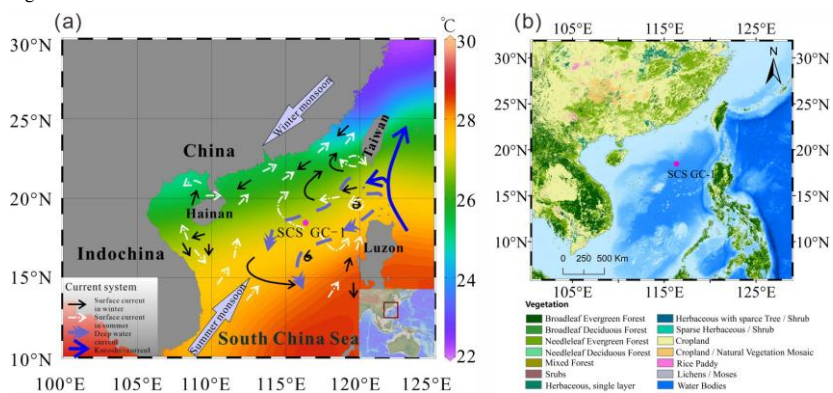
28 **1 Introduction**

29 Low latitude regions play a critical role in the global climate and its dynamic because they are the seat of the most active
30 moisture and heat exchanges between the atmosphere and the ocean expressed via the monsoon regime. Tropical and
31 subtropical monsoon regions such as East Asia and the South China Sea (SCS) experience the most significant seasonal
32 reversal in wind directions with associated migration of regional intense precipitation (Wang et al., 2017). Monsoon wind and
33 precipitation patterns have changed significantly in the late Quaternary, influenced by gradual changes in insolation and
34 internal interactions among the atmosphere, oceans, land surfaces and Northern Hemisphere ice sheets (An, 2000; Ding et al.,
35 1994; Kissel et al., 2020; Tian et al., 2010; Wang et al., 2001). These changes have affected the climate and land-ocean energy
36 balance of western Pacific marginal basins, whereas the influence and dynamics of the monsoon system remain insufficiently
37 constrained. Investigations of palaeoclimate variability have significant value in providing valuable insights into monsoonal
38 dynamics across tectonic, orbital and millennial time scales.

39 Given the importance of the climate signature during the last Glacial Maximum (LGM, spanning approximately 26.5-19 ka)
40 to climate model validation and testing, new reconstructions of precipitation and vegetation response during the LGM are

41 necessary to resolve inconsistencies and improve model reliability. Marine sediments potentially record the interplay of the
 42 East Asian Monsoon, surface and deep oceanic circulation and sea level compared with other terrestrial records (Tian et al.,
 43 2004; Wang et al., 1999). The South China Sea is divided into a northern deep basin with isolated, oxygen-poor waters and a
 44 southern extensive shelf province, a dichotomy fundamentally controlled by a ~2400 m deep sill that restricts deep-water
 45 exchange with the open Pacific (Chen and Huang, 1996). Due to its well-preserved sedimentary strata, abundant sediment
 46 supply, and relatively high sedimentation rates, the northern SCS is recognized as a key area with strong potential for high-
 47 resolution palaeoenvironmental reconstructions. Such records can substantially enhance our ability to resolve global and
 48 regional climate variability during the Quaternary (Wang et al., 2014). A range of different proxies is preserved in marine
 49 sedimentary archives. Pollen evidence, for example, can provide a valuable signal of vegetation evolution on the adjacent
 50 continental land mass (Cheng et al., 2023; Luo et al., 2016; Sun et al., 2000a), while microcharcoal particles are widely used
 51 in palaeofire reconstruction to infer fire frequency, intensity and vegetation changes, and terrestrial ecosystem response
 52 (Conedera et al., 2009). Foraminifera are sensitive to environmental changes, and are widely applied as a palaeo-proxy of
 53 marine conditions (Haynes, 1981), although the shells of planktonic foraminifera are susceptible to dissolution which may
 54 have limitations. Organic walled dinoflagellate cysts (dinocysts), the resting cysts formed during the sexual reproduction
 55 process of these taxa, are characterized by resistant organic matter and are also generally well preserved in marine sediments
 56 (Dale, 1996; Zonneveld et al., 2013). The well-known correlation of modern dinocyst distribution with distinct physical marine
 57 water properties such as sea surface temperature (SST), salinity, nutrients and productivity indicates the value of dinocysts as
 58 a proxy in palaeoceanographic reconstruction, although current research on dinocysts in the South China Sea remains largely
 59 confined to their modern distribution in marine surface sediments (Li et al., 2018a; Li et al., 2020; Li et al., 2023). Fossil
 60 dinocyst records in the SCS are scarce (Li et al., 2021; Li et al., 2017).

61 While previous studies have documented glacial-interglacial changes in vegetation and oceanography in the northern SCS, the
 62 relative importance of different forcing mechanisms-particularly the high- and low-latitude forcing across these transitions
 63 remain uncertain. To address this, we adopt a multi-proxy approach in this study, combining palynological indicators (pollen,
 64 spores, microcharcoal, and dinocysts), organic geochemical proxies (TOC and TN), and inorganic geochemical markers
 65 (element ratios, $\delta^{13}\text{C}$ and $\delta^{18}\text{O}$, and Mg/Ca-based SST of planktonic foraminifera) to reconstruct vegetation, fire regimes,
 66 sediment sources, ocean productivity, and sea surface temperature. A marine sediment core (SCS-GC-1; Fig. 1a) recovered
 67 from the northern SCS was analyzed to reconstruct millennial-scale climate and ocean dynamics over the last 33 ka. The
 68 specific aims of this study are: (1) to reconstruct the palaeovegetation and palaeoclimate; (2) to document the evolution of
 69 palaeoceanographic conditions; and (3) to clarify how land-ocean interactions and dominant climate forcings shift across
 70 glacial-interglacial transitions.



71
 72 **Figure 1:** (a) Map of the East Asian monsoon system and ocean circulations with annual modern mean annual sea surface
 73 temperature (Data from World Ocean Atlas, 2023) and the location of core SCS GC-1 (red) retrieved from the northern SCS.

74 (b) Map of the distribution of vegetation types in the main areas around the South China Sea retrieved from Stibig et al. (2007)
75 and <https://forobs.jrc.ec.europa.eu/products/glc2000/products.php>. The black solid line indicates the position of the winter
76 surface current, the white dashed line is the position of the summer surface current, the purple dashed line is the deep current,
77 and the blue solid line is the Kuroshio Current.

78 2 Environmental setting

79 2.1 Atmospheric circulation and climate

80 The northern SCS experiences a subtropical to tropical climate with high temperatures (15-28°C annually): the mean air
81 temperatures range from 15-25°C during the coldest month (January), and ~28°C during the warmest month (July). Rainfall
82 is copious with an annual mean of 1000-2000 mm (Li et al., 2017). The climate is primarily governed by the seasonal East
83 Asian Monsoon system: northeasterly winds prevail during winter (December-February) and southwesterlies dominate in
84 summer (June-August) (Chao et al., 1995; Wang et al., 2017). In winter, decreasing temperatures over the Asian continent lead
85 to the development and intensification of a cold high-pressure system over Inner Mongolia, while the Aleutian Low strengthens
86 over the North Pacific. The resulting continent-ocean pressure gradient drives the East Asian Winter Monsoon (EAWM),
87 transporting cold, dry northeasterly air masses southwards across China into the SCS. In summer, this pattern reverses: the
88 continental system is replaced by the Indian Low, and stronger high-pressure systems develop over the North Pacific and the
89 Australian region, generating the East Asian Summer Monsoon (EASM), which advects warm, moist-laden air from the ocean
90 onto the Chinese mainland (Liu et al., 2016a).

91 2.2 Oceanic circulation

92 Surface currents in the SCS are controlled by seasonal variations in the dominant wind directions related to the EASM and
93 EAWM (Hu et al., 2000), monsoon-topography interactions, and additional influences from wind-stressed eddies. During
94 winter, the EAWM drives a strong southward western boundary current along the Vietnamese and southern Chinese coasts,
95 associated with a basin-scale cyclonic circulation. In contrast, summer circulation is weaker and more complex, with coastal
96 currents generally reversing to flow northward under EASM influence.

97 The EASM drives distinct northern and southern circulation patterns in the SCS, which form two anticyclonic eddies separated
98 near 12°N by a strong upwelling off Vietnam (Fang et al., 1998). In addition, the region is influenced by the intrusion of warm,
99 saline Kuroshio waters entering through the Luzon strait between Luzon from Taiwan (Huang et al., 2025).

100 Seasonal variations in marine primary productivity are primarily modulated by the East Asian Monsoon (Liu et al., 2002).
101 During winter, stronger northeasterlies induce eutrophic conditions in the upper euphotic layer, elevating marine primary
102 productivity. In summer, persistent heating of warmer, lower-density surface waters intensifies stratification, leading to
103 oligotrophic conditions and reduced primary productivity (Liu et al., 2002; Zhang et al., 2016).

104 2.3 Vegetation

105 Vegetation types on the adjacent continental landmass around the SCS are diverse and reflect regional climate conditions (Luo
106 and Sun, 2013), although they are dominated by tropical and subtropical broadleaved evergreen forests (Fig. 1b) (Stibig et al.,
107 2007). Whereas tropical rain forest vegetation, characterized by taxa such as Dipterocarpaceae, Moraceae, Sapindaceae and
108 Sapotaceae, occurs at low altitudes on tropical islands along the southern coast of the Chinese mainland, e.g., Hainan Island,
109 and southern Taiwan Island. Tropical monsoon forests are distributed widely throughout the Indochina Peninsula and along
110 the coast of southeastern China with the representative species including Verbenaceae, Dipterocarpaceae, as well as pine trees
111 (including *Pinus merkusii*, *Pinus kesiya*, and *Pinus insularis*) which are dominant in the composition of monsoon mountain
112 forest. Subtropical evergreen forests, mainly composed of the families Fagaceae (e.g., *Cyclobalanopsis* and *Quercus*),
113 Lauraceae, and Theaceae, Hamamelidaceae and Magnoliaceae are prominent between 24°N and 25°N on southeast-facing
114 hills and on high plateaus (Wang, 1961; Whitmore, 1985). Generally, the abundance of both tropical and subtropical taxa

115 increase gradually towards the south in eastern China, indicating the significance of the north-south temperature gradient (Dai
116 and Weng, 2015; Dai et al., 2015).

117 ~~The SCS receives enormous amounts of terrigenous sediments (ca. 700×10^6 tons/year) every year, delivered mainly during the~~
118 ~~rainy season in summer. The sediments originate from the erosion/weathering of rocks in the catchment basins particularly~~
119 ~~from via three major Asian river systems: (the Red River, the Pearl River, and the Mekong River) which are among the largest~~
120 ~~in the world (Liu et al., 2010; Milliman and Syvitski, 1992). Among these, the Pearl River, located northeast of the core site,~~
121 ~~represents a particularly important pathway for transporting terrestrial palynomorphs (including pollen, spores and charcoal)~~
122 ~~from the adjacent continents to the deep basin. Beyond the river deltas, part of the terrigenous sediments is deposited on the~~
123 ~~shelves (Zhong et al., 2017), while the rest reaches the open sea where the sediment is transported by the oceanic currents and~~
124 ~~deposited on the continental slope and in the deep basins (Liu et al., 2013). Consequently, The~~ vegetation types occurring in
125 southeast and southern China, as well as Taiwan Island, are the main pollen sources of the northern SCS (Dai and Weng, 2011;
126 Sun et al., 1999).

127 **2.4 Sedimentation rates**

128 ~~The SCS receives enormous amounts of terrigenous sediments (ca. 700×10^6 tons/year) every year, mainly during the rainy~~
129 ~~season in summer. The sediments originate from the erosion/weathering of rocks in the catchment basins particularly from~~
130 ~~three Asian rivers (the Red River, the Pearl River, and the Mekong River) which are among the largest in the world (Liu et al.,~~
131 ~~2010; Milliman and Syvitski, 1992). Beyond the river deltas, part of the terrigenous sediments is deposited on the shelves~~
132 ~~(Zhong et al., 2017), while the rest reaches the open sea where the sediment is transported by the oceanic currents and deposited~~
133 ~~on the continental slope and in the deep basins (Liu et al., 2013).~~

134 **3. Materials and methods**

135 **3.1 Materials and chronological analysis**

136 The 305 cm long marine sediment core SCS GC-1 was retrieved from the northern SCS during R/V Songhang (Shanghai
137 Ocean University) cruise in October 2022 (18.47°N, 116.34°E; water depth of 3764 m) (Fig. 1).

138 Eight accelerator mass spectrometry AMS ^{14}C dates at depths of 20 cm, 45 cm, 65 cm, 90 cm, 107 cm, 133 cm, 203 cm and
139 275 cm were obtained on mixed planktic foraminiferal (including *Globigerinoides ruber*, *Globigerinoides sacculifer*,
140 *Neoglobobadrina dutertrei*, *Pulleniatina obliquiloculata*, *Orbulina universa*) tests isolated from the core. AMS ^{14}C
141 measurements were carried out on a NEC 0.5Mev ^{14}C AMS (National Electrostatics Corporation, NEC) at Guangzhou Institute
142 of Geochemistry, Chinese Academy of Sciences (GIGCAS).

143 **3.2 X-ray fluorescence (XRF) analysis**

144 The core was non-destructively scanned using the Avaatech XRF Core Scanner at the State Key Laboratory of Marine Geology,
145 Tongji University. The parameters of the Avaatech XRF core scanner were set for 30 s exposure time, three voltage and current
146 conditions with 10 kv and 0.75 mA for Al-Fe, 30 kV and 0.5 mA for Co-Mo, and 50 kV and 0.2 mA for Tc-U. The scanning
147 area was 5 mm (length) \times 10 mm (width), and at a scanning time of 30 s. The relative content of each element including Al to
148 Ba which was obtained, is expressed in cps as counts per second.

149 **3.3 TOC and TN analysis**

150 Approximately 1 g of each freeze-dried sample was treated with diluted 3 mol/L HCl for 24 hours at room temperature to
151 remove inorganic carbonates. After the reaction, the samples were repeatedly rinsed with ultrapure water ($>18 \text{ M}\Omega \cdot \text{cm}$) and
152 centrifuged until the supernatant reached a neutral pH. The remaining residue was oven-dried at 60°C, ground and then
153 weighed. The decarbonated samples were analyzed for elemental content using a Vario EL cube elemental analyzer (Elementar,

Field Code Changed

154 Germany) at the State Key Laboratory of Marine Geology, Tongji University, employing the dry combustion method.
155 Replicate analyses were conducted to ensure data reliability, with average standard deviations of ≤ 0.1 wt% for both TOC and
156 TN measurements.

157 3.4 Planktonic foraminiferal isotopic and Mg/Ca analysis

158 The samples were freeze-dried, disaggregated by soaking in water for 1-2 days, then were rinsed repeatedly through a 63 μm
159 sieve to remove organic matter and fine impurities. The rinsed wet samples were then dried at 60°C (approximately 24 h) and
160 passed through a 125 μm and 250 μm sieve, respectively (Schönfeld et al., 2012). *G. ruber* larger than 250 μm size were
161 selected under a microscope. For each sample, clean and intact *G. ruber* (around 30 specimens) were picked and tested using
162 a Finnigan MAT253 Mass Spectrometer. The $\delta^{18}\text{O}$ results are reported versus VPDB after calibration with NBS 19. The
163 average test accuracy is $\pm 0.07\%$.

164 For the Mg/Ca analysis, surface dwelling foraminiferal species with smooth-surface individuals of *G. ruber* between 250-350
165 μm (ca. 0.3 mg) were picked to ensure no obvious contamination or damage, and that the atrioventricular structure was intact
166 (Barker et al., 2003). The analysis was performed on a quadrupole inductively coupled plasma mass spectrometry (ICP-MS).
167 Duplicate measurements of two samples yield an average relative deviation of 0.064 mmol/mol, confirming that analytical
168 uncertainty is minimal and does not materially affect interpretation. Sea surface temperatures were reconstructed following
169 Eq. (1) (Huang et al., 2008):

$$170 SST = 0.5 * (\ln(Mg/Ca/0.3)/0.09 + \ln(Mg/Ca/(0.38 - 0.02 * D)))/0.09 \quad (1)$$

171 Where *SST* represents mean annual sea surface temperature (°C), *Mg/Ca* is the *G. ruber* based Mg/Ca ratio (mmol/mol), *D* is
172 water depth of the core (km).

173 3.5 Palynological analysis

174 In total, 61 samples (mean interval 4 cm) were processed for palynological analysis at Shanghai Ocean University following
175 standard preparation procedures. Samples were treated sequentially with 10% HCl, 40% HF, 30% HCl, sieved with 125 μm
176 and 7 μm meshes, and mounted for microscopic examination. Routine identification was performed under a light microscope
177 (ZEISS Promostar 3) at 400x magnification, with 1000x used for detailed taxonomic identification. Four *Lycopodium* spore
178 tablets with 10315 \pm 845 spores were added to each sample prior to processing to enable calculation of pollen concentration.
179 Pollen taxa were identified using the reference of Tang et al. (2020). At least 300 pollen grains (including terrestrial pollen
180 taxa, sedges and aquatic taxa) were counted for most of the samples. The percentages of pollen taxa were calculated based on
181 the pollen sum excluding *Pinus*, and the percentages of spore taxa were calculated based on pollen and spore sum. The 95%
182 confidence intervals of percentages were calculated following Maher (1972).

183 Charcoal particles were identified and counted on the same microscope slides prepared for pollen analysis. Only particles
184 which were black, opaque and angular were considered as charcoal. Particles smaller than 10 μm were not counted due to the
185 risk of false identification (Mooney and Tinner, 2011). More than 1500 charcoal particles (with an average of 3500 particles)
186 were counted for each sample. Two size classes were defined, based on the length of the long axis of each fragment: 10-100
187 μm is assumed to relate to the regional fire signal and >100 μm to local fire signals (Conedera et al., 2009).

188 Organic-walled dinoflagellate cysts (dinocysts) were identified based on Zonneveld et al. (2013), DINOFLAJ3 (Williams et
189 al., 2017), and the online modern dinocyst determination key, viz Zonneveld and Pospelova (2015) and references therein. The
190 percentage of each taxon was calculated based on the total number of dinocysts. The 95% confidence intervals of percentages
191 were calculated following Maher (1972). All identified dinocyst taxa and their motility affinities are listed in Table S1. In
192 addition to the above content, foraminiferal organic linings, and other non-pollen palynomorphs such as fungal spores were
193 counted. All counts of pollen, microcharcoal and dinocysts as well as other data discussed in this study have been submitted
194 in the Pangaea database (<https://pangaea.de>) (Felden et al., 2023).

195 3.6 Statistical analysis

196 The pollen and dinocyst data were analyzed statistically using the CANOCO software (Canonical Community Ordination:
197 version 5) (ter Braak and Smilauer, 2012). The percentage data used for statistical analysis was not transformed. A Detrended
198 Correspondence Analysis (DCA) was first conducted to test the distribution of the dataset (unimodal or linear). The longest
199 gradient of DCA analysis was found to be 1.1 for pollen data and 1.5 for dinocyst data with standard deviations both less than
200 3, suggesting that the linear model is more suitable. Accordingly, separate Principal Component Analysis (PCA) were
201 performed to determine the relationship between relative abundances of pollen and dinocyst taxa. Assemblage zones were
202 determined using the constrained cluster analysis (CONISS) in the TILIA (3.0.1) software (Grimm, 2015), which were
203 performed separately, for the pollen (based on a sum excluding *Pinus*) and dinocyst taxa. The top two samples were excluded
204 from the dinocyst CONISS analysis due to insufficient dinocyst counts .

205 4. Results

206 4.1 Age-depth model

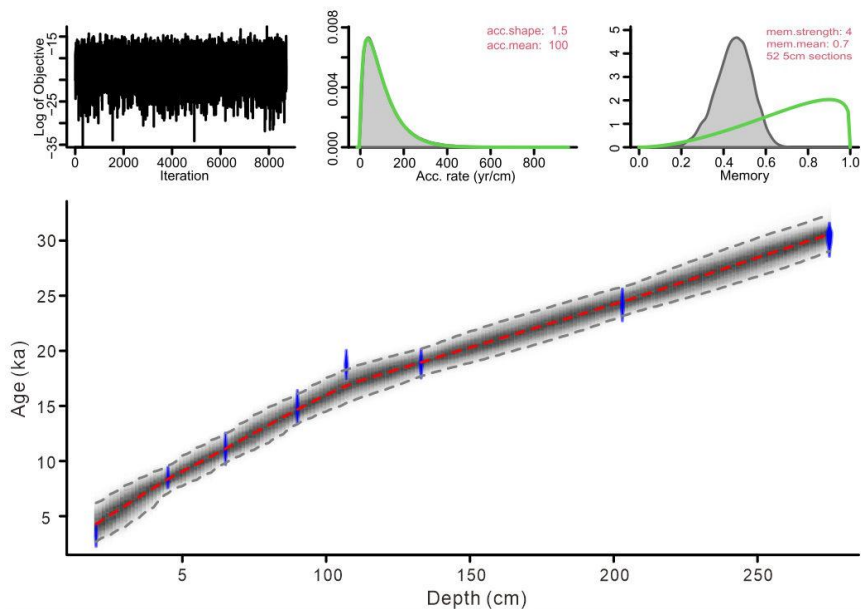
207 The eight ^{14}C AMS measurements exhibit a systematic increase in radiocarbon age with sediment depth (Table 1). The age-
208 depth model was constructed using the eight AMS ^{14}C measurements in a Bayesian framework implemented in Bacon (Blaauw
209 and Christen, 2011). A prior accumulation rate of 100 yr/cm (shape = 1.5, normal distribution) was applied, with the core
210 divided into 52 depth sections of 5 cm. The default memory parameter was retained. Posterior weighted mean calibrated ages
211 were used to derive linear sedimentation rates. The resulting model indicates a basal age of ~33 ka for core SCS GC-1, with
212 sedimentation rates ranging between 0.005 and 0.013 cm/yr (Figs. 2 and 3a).

213

214 **Table 1:** AMS ^{14}C measurement for mixed planktonic foraminifera from the core SCS GC-1.

Lab #	Depth (cm)	Material	^{14}C age (yr BP)	Calibrated age median (cal. yr BP)	cal. ^{14}C age (cal. yr BP, $\pm 2\sigma$)
GZ10650	20	mixed species	3420 \pm 25	3036	1810-4285
GZ10651	45	mixed species	8005 \pm 35	8289	7260-9443
GZ10652	65	mixed species	10055 \pm 50	10868	9533-12260
GZ10653	90	mixed species	13090 \pm 70	14708	13392-16057
GZ10654	107	mixed species	15950 \pm 70	18342	17138-19485
GZ10655	133	mixed species	16000 \pm 90	18399	17185-19555
GZ10656	203	mixed species	20540 \pm 170	23656	22496-24875
GZ10657	275	mixed species	26700 \pm 350	29977	28806-31063

215 # yr BP denote before present (1950 AD); all age data were calibrated using the software Calib.Rev.8.10 (Stuiver and Reimer,
216 1993) and Marine 20 (Hughen et al., 2004). The standard marine reservoir age with a local modification ($\Delta R = 71 \pm 499$ yr) in
217 the northern South China Sea was applied (Wan and Jian, 2014).

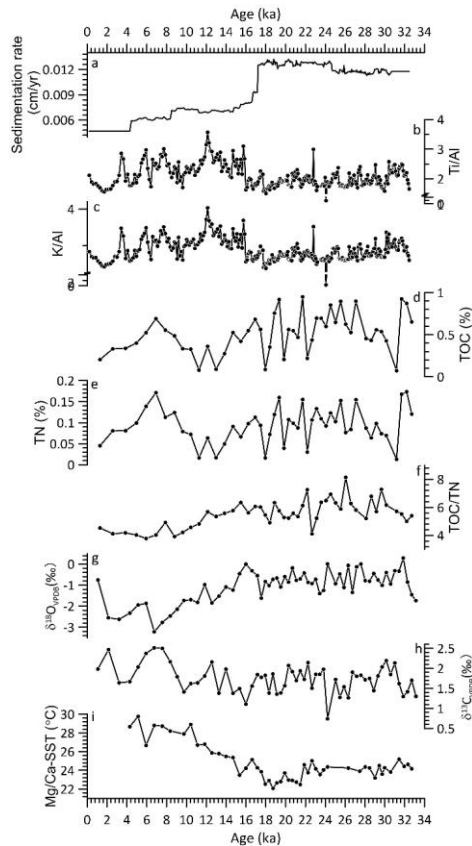


218

219 **Figure 2:** Bayesian age-depth model based on eight AMS ^{14}C dates from core SCS GC-1: the blue areas represent the 95%
 220 probability distributions of the calibrated ages; the thin red line shows the weighted mean ages, and the blackish-gray area
 221 shows the 95% age-depth relations as modeled by the R software package Bacon 2.2 (Blaauw and Christen, 2011).

222 4.2 XRF record

223 The relative contents of these six elements are found for Fe (5×10^3 - 750×10^3 cps, mean = 540×10^3 cps), Ca (0.7×10^3 - 650×10^3
 224 cps, mean = 190×10^3 cps), K (1.5×10^3 - 166×10^3 cps, mean = 91×10^3 cps), Si (1×10^3 - 144×10^3 cps, mean = 71×10^3 cps)
 225 followed by Ti (2×10^3 - 68×10^3 cps, mean = 41×10^3 cps) and Al (0.5×10^3 - 14×10^3 cps, mean = 6×10^3 cps) (Fig. S1). Similar
 226 patterns among terrigenous elements Fe, K, Ti, Al and Si were observed together with a clearly opposite pattern of marine
 227 origin element Ca. The Ti/Al and K/Al show similar patterns with significant correlation ($r = 0.94$, $P < 0.001$) throughout the
 228 record (Figs. 3b and 3c), with low values prior to 16 ka and then increase quickly to much higher values after 16 ka with
 229 gradually decreasing trend to the end of the record.



230

231 **Figure 3:** Core SCS GC-1 sedimentation rate (a), major element ratio (b-c), contents of total organic carbon (TOC, d) and
 232 nitrogen (TN, e), TOC/TN ratio (f), stable oxygen isotope $\delta^{18}\text{O}_{\text{VPDB}}$ (g) and stable carbon isotope $\delta^{13}\text{C}_{\text{VPDB}}$ (h) isotopes **of** from
 233 planktic foraminifera, and Mg/Ca-SST (i).

234 4.3 TOC, TN and TOC/TON record

235 TOC content and the TOC/TN ratio exhibit significant fluctuations throughout the record (Figs. 3d, 3e and 3f). The period
 236 prior to 14.7 ka is characterized by high TOC content with low values around 31.2 ka, 22.2 ka, 19.8 ka, 17.9 ka. After 14.7 ka,
 237 TOC decreased until 10.4 ka when it increased again to a high level around 6.9 ka followed by a decline trend until the top of
 238 the record. Similarly, TOC/TN ratio also exhibits high values prior to 14.7 ka, which then decreased to minimum between 8.8-
 239 5.9 ka interrupted by a brief increase around 7.9 ka.

240 **4.4 Planktonic foraminiferal isotopic and Mg/Ca-SST record**

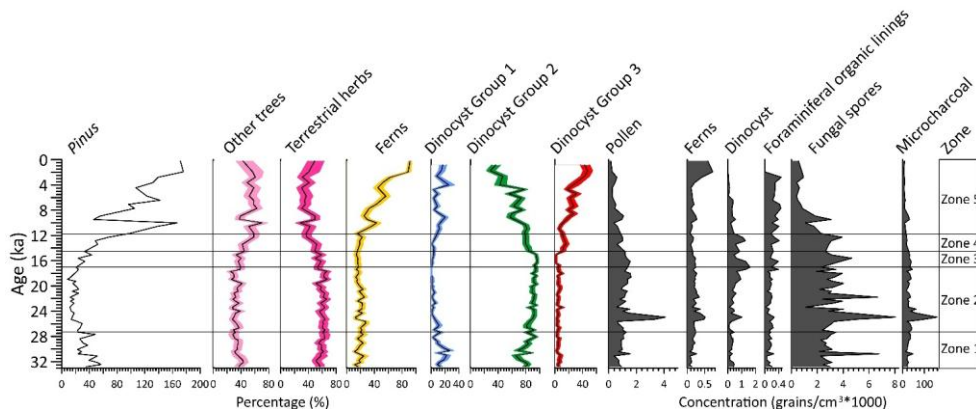
241 The $\delta^{18}\text{O}$ values of planktonic foraminifera *G. ruber* shells range from -3.2‰ to 0.3‰ (mean= -1.1‰) with higher values
242 prior to 18.7 ka, then started decreasing to much lower values with a short decline around 17.5-14.7 ka (Fig. 3g). The $\delta^{13}\text{C}$
243 values range from 0.7‰ to 2.5‰ (mean= 1.7‰) with relatively low values prior to 16 ka (Fig. 3h), there after increasing but
244 with substantial variation.

245 Mean Mg/Ca-derived SSTs range from 22.1°C to 29.7°C (mean = 24.8°C) across the core (Fig. 3i). Relatively low values
246 ($23.2\text{-}25.2^{\circ}\text{C}$, mean = 24.2°C) occur prior to 21.9 ka, followed by a further decline to the lowest values ($22.1\text{-}24.6^{\circ}\text{C}$, mean =
247 23.1°C) between 21.9-17.5 ka. After 17.5 ka, SSTs increase progressively toward the highest values observed in the record
248 ($23.5\text{-}29.7^{\circ}\text{C}$, mean = 26.8°C) with a short decline around 16.6-14.7 ka .

249 **4.5 Palynological record**

250 The complete diagrams of pollen, dinocyst percentages and concentrations, and charcoal results are shown in Figs. S2-S6.
251 Pollen concentration is variable, with particularly high concentrations ($390\text{-}4100$ grains/ cm^3 ; mean = 1200 grains/ cm^3) prior
252 to 16.1 ka, and highest concentrations around 25.3-25.0 ka ($3300\text{-}4100$ grains/ cm^3 ; mean = 3700 grains/ cm^3) (Fig. 4). Similarly,
253 charcoal exhibits the highest concentrations ($36\text{-}155 \times 10^3$ particles/ cm^3 ; mean = 83×10^3 particles/ cm^3) around 25.3-23.7 ka,
254 decreasing after 15.6 ka, reaching minimum values at the top of the core ($9\text{-}31 \times 10^3$ particles/ cm^3 ; mean = 21×10^3 particles/ cm^3)
255 (Figs. 4 and S6). Dinocyst concentrations are relatively low, ranging from $7\text{-}1600$ cysts/ cm^3 (average of 450 cysts/ cm^3) with
256 high values of $110\text{-}1600$ cysts/ cm^3 (average of 650 cysts/ cm^3) between 25.6-11.7 ka (Figs. 4 and S5). After 11.7 ka, dinocyst
257 concentrations decrease, reaching a minimum at the end of the record.

258

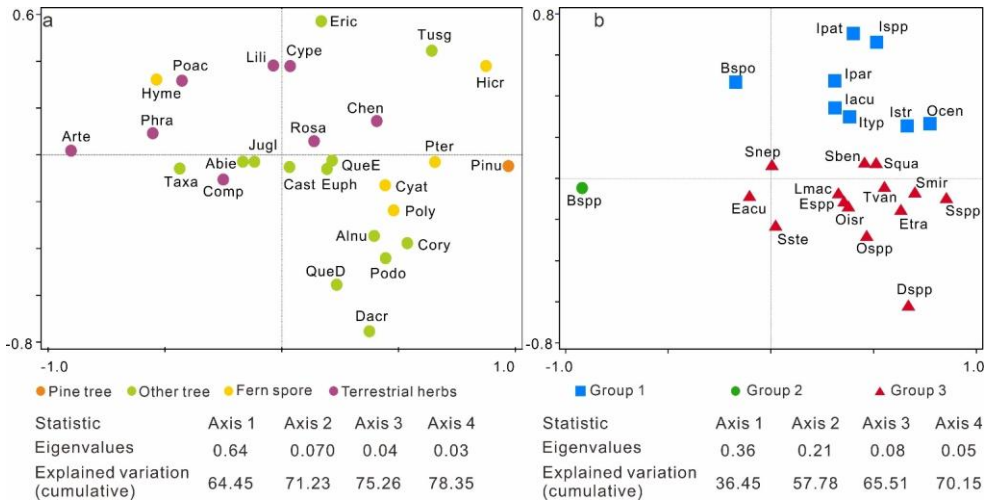


259

260 **Figure 4:** Percentages (%) of dominated pollen taxa, including pollen of *Pinus*, other trees, terrestrial herbs, fern spores, and
261 three dinocyst groups based on principal component analysis (PCA) analysis, concentrations (grains/ $\text{cm}^3 \times 1000$) of pollen, fern
262 spores, dinocyst, foraminiferal organic linings, fungal spores and microcharcoal concentration (particles/ $\text{cm}^3 \times 1000$).

263 According to the PCA results (Fig. 5a), pollen and spore taxa are well-separated based on their associated biomes. Specifically,
264 *Pinus* and fern spore (notably *Hicriopteris*, *Pteris*, Polypodiaceae and Cyathaceae) form a distinct cluster on the positive end
265 of axis 1, while characteristic terrestrial herbs (particularly *Artemisia*, Poaceae and Cyperaceae) are separated along the
266 negative end of axis 1 and relatively positive side of axis 2. Three groups of dinocyst taxa can be distinguished based on the

267 PCA results, showing clearly different trends across the record (Fig. 5b). Group 1: *Operculodinium. centrocarpum*,
 268 *Impagidinium* spp., *Impagidinium aculeatum*, *Impagidinium patulum*, *Impagidinium paradoxum*, *Impagidinium strialatum*,
 269 *Impagidinium* type1; *Bitectatodinium spongium*; Group 2: *Brigantedinium* spp.; Group 3: *Echinidinium* spp., *Echinidinium*
 270 *aculeatum*, *Echinidinium transparentum*, *Selenopemphix nephroides*, *Stellasinium stellatum*; *Selenopemphix quanta*,
 271 *Dubridinium* spp., *Operculodinium israelianum*; *Operculodinium* spp., *Lingulodinium machaerophorum*, *Tuberculodinium*
 272 *vancampoeae*, *Spiniferites mirabilis*, *Spiniferites* spp.; *Spiniferites bentori*.



273
 274 **Figure 5:** Results of the principal component analysis (PCA) illustrating the ordination of pollen (a) and dinocyst taxa (b) from
 275 core SCS GC-1 with colored symbols referring to the groups. For pollen, pine tree (orange): Pinu (*Pinus*); other tree (light
 276 green): QueE (*Quercus* evergreen), QueD (*Quercus* deciduous), Alnu (*Alnus*), Podo (Podocarpaceae), Dacr (*Dacrycapus*),
 277 Taxa (Taxaceae), Abie (*Abies*), Tusc (*Tusga*), Eric (Ericaceae), Jugl (*Juglans*), Cory (*Corylus*), Cast (*Castanea*), Euph
 278 (Euphorbiaceae); fern spores (yellow): Hicr (*Hicriopteris*), Pter (*Pteris*), Cyat (Cyatheaceae), Poly (Polypodiaceae), Hyme
 279 (Hymenophyllaceae); terrestrial herbs (purple): Arte (*Artemisia*), Poac (Poaceae), Cype (Cyperaceae), Comp (Compositae),
 280 Phra (*Phragmites*), Chen (Chenopodiaceae), Rosa (Rosaceae), Lili (Liliaceae). For dinocyst groups, Group 1 (blue): Ocen (*O.*
 281 *centrocarpum*), Ispp (*Impagidinium* spp.), Iacu (*Impagidinium aculeatum*), Ipat (*Impagidinium patulum*), Ipar (*Impagidinium*
 282 *paradoxum*), Istr (*Impagidinium strialatum*), Ityp (*Impagidinium* type1), Bspo (*Bitectatodinium spongium*); Group 2: Bsp
 283 (*Brigantedinium* spp.); Group 3: Esp (Echinidinium spp.), Eacu (*Echinidinium aculeatum*), Etra (*Echinidinium*
 284 *transparentum*), Snep (*Selenopemphix nephroides*), Sste (*Stellasinium stellatum*), Squa (*Selenopemphix quanta*), Dsp
 285 (*Dubridinium* spp.), Oisr (*Operculodinium israelianum*), Ospp (*Operculodinium* spp.), Lmac (*Lingulodinium*
 286 *machaerophorum*), Tvan (*Tuberculodinium vancampoeae*), Sben (*Spiniferites bentori*), Smir (*Spiniferites mirabilis*), Ssp
 287 (*Spiniferites* spp.).

288 Separate CONISS analysis were performed for pollen and dinocyst data, with results shown in Figs. S2 and S4. Considering
 289 that the zonations based on pollen and dinocyst data show very similar results, five main zones can be recognized in the record
 290 for the purpose of synthesizing the multi-proxy climatic signal (Fig. 4):

291 **4.5.1 Zone 1 (301-237cm, 32.8-27.3 ka)**

292 This zone is characterized by relatively high percentages of *Pinus* and evergreen *Quercus*, while pollen taxa of terrestrial herbs
293 such as *Artemisia*, Poaceae and Cyperaceae as well as fern spores including *Hicriopteris*, Polypodiaceae, Cyathaceae are
294 relatively low (Figs. 4 and S2). High fungal spore concentrations here coincide with low charcoal concentrations. The
295 percentages of heterotrophic taxa *Brigantedinium* spp. (Group 1) increase gradually to the end of this zone, whereas the
296 percentages of autotrophic taxa (Group 2) particularly *Impagidinium* species reach their maximum levels in the record but
297 decline towards the end of this phase (Figs. 4 and S4). Concentrations of foraminiferal organic linings reach minimum in this
298 zone.

299 **4.5.2 Zone 2 (237-109 cm, 27.3-17.0 ka)**

300 The percentage of *Pinus* pollen decreases to its lowest values of the entire record. Meanwhile, terrestrial herb taxa, particularly
301 *Artemisia*, increase to their highest levels along with fungal spores. Some fern spore types, including Polypodiaceae,
302 Hymenophyllaceae, Cyatheaceae and *Pteris*, also exhibit relatively high values compared to Zone 1 (Figs. 4 and S2).
303 Concentrations of pollen, fern spores and charcoal all reach maximum values, peaking around 25.3-24.3 ka when dinocyst
304 concentrations also exhibit a maximum, along with *Brigantedinium* spp. On the other hand, Group 1 dinocyst taxa are at
305 minimum values in this zone. Concentrations of foraminiferal organic linings remain at low value in this zone.

306 **4.5.3 Zone 3 (109-89 cm, 17.0-14.5 ka)**

307 ~~In comparison to Zone 2, Zone 3 is marked by a slight increase of *Pinus* and decrease in herb pollen. Both pollen and charcoal~~
308 ~~concentration exhibit slight decreasing trend. Concentrations of fungal spores exhibit a declining trend and return to the levels~~
309 ~~observed in Zone 1. Dinocyst concentrations quickly decrease to relatively low values. While *Brigantedinium* spp. remain high~~
310 ~~values, other taxa such as *Echinidinium* spp., *Echinidinium aculeatum* and *Spiniferites* species exhibit minimum values.~~

Formatted: Normal

Formatted: Font: Italic

311 **4.5.4 Zone 4 (109-89 cm, 17.0-14.5 ka)**

312 ~~CONISS analysis suggests a sub-zone (zone 3) around 17.0-14.5 ka which is marked by a further decline of *Pinus* and increase~~
313 ~~in herb pollen. Then Zone 4 is characterized by the rapid increase in *Pinus* pollen, accompanied by a sharp decline in terrestrial~~
314 ~~herbs, especially *Artemisia*. Concentrations of fungal spores exhibit a declining trend and return to the levels observed in Zone~~
315 ~~1. Concentrations of pollen, fern spores and charcoal also exhibit a declining trend to reach near the lowest levels, whereas~~
316 ~~dinocyst concentrations remain relatively prominent. However, the percentage of *Brigantedinium* spp. exhibits a decline in~~
317 ~~this zone, accompanied by a marked increase of Group 3 taxa, including *Dubridinium* spp. and *Echinidinium* spp. Meanwhile,~~
318 ~~dinocysts in Group 2 achieve relatively high values. Concentrations of foraminiferal organic linings increase gradually from~~
319 ~~the beginning of this zone.~~

320 **4.5.5 Zone 5 (69-0 cm, 11.7 ka-present)**

321 The percentages of *Pinus* pollen reach their highest values of the entire record interrupted around 9.5-9.0 ka by a very marked
322 decline to values close to those of Zone 1. The abrupt reduction in *Pinus* pollen is also observed in the overall pollen, fungal
323 spore, charcoal concentration, and in terrestrial herb pollen especially. Additionally, this zone is characterized by the increase
324 in fern spores, particularly *Hicriopteris* which exhibits a short, sharp increase around 2.8 ka (Figs. 4 and S2). The percentage
325 of *Brigantedinium* spp. decreases to the lowest values of the entire record, whereas the percentage of Group 3 dinocyst taxa,
326 along with the concentration of foraminiferal organic linings all reach their highest values.

327 5. Discussion

328 5.1 Environmental significance of key proxies

329 5.1.1 K/Al and Ti/Al

330 In comparison to single elements, elemental ratios which are insensitive to dilution effects, are more useful as environmental
331 indicators (Govin et al., 2012). Ti is highly enriched in mafic and volcanic rocks, while Al is a major component of most
332 common clay mineral found in all types of weathered continental crust. The SCS is surrounded by diverse geological terrains
333 with distinct Ti/Al ratios originating from different sources such as the Luzon Volcanic Arc (Philippines), Taiwan and other
334 basaltic sources with high Ti/Al, while with low Ti/Al originating from the major continental river systems that drain ancient,
335 weathered landmasses. Thus, Ti/Al can provide a robust picture of terrestrial input and its origin in the complex environment
336 of the SCS. High Ti/Al indicates increased relative input of sediment from a volcanic or mafic source/less chemical, and low
337 Ti/Al indicates increased relative input of sediment from a felsic continental source (e.g., Pearl River, Mekong River) (Hu et
338 al., 2013; Wan et al., 2007). K/Al and Ti/Al records of ODP Site 1143 from the SCS generally show low values during glacial
339 periods and high values during interglacial periods, clearly indicating that increase in K/Al and Ti/Al is probably related to
340 wetter conditions and thus the intensified chemical weathering (Clift et al., 2008; Tian et al., 2011; Wei et al., 2004).

341 5.1.2 Source area and transport of pollen and spores

342 In the northern SCS sediments, the modern distribution of tree pollen, particularly *Pinus*, shows disproportionately high
343 representation relative to other pollen types. This suggests substantial contributions from south and southeast China,
344 transported primarily by the northeasterly winter monsoon and associated wind-driven currents. While elevated *Pinus*
345 percentages can signal either a strengthened winter monsoon or a cool, humid climate (Luo et al., 2018; Sun et al., 2003), PCA
346 results (Fig. 5a) indicate that this ambiguity can be resolved by incorporating fern spore data. Unlike wind-dispersed *Pinus*
347 pollen, the larger, heavier spores of ferns are primarily transported by river runoff. Their high abundance in sediments therefore
348 signals a proximal source from humid montane forests (e.g., in Taiwan and southern China), reflecting a humid climate
349 controlled by the EASM (Kaars et al., 2000; Sun et al., 2000b; Wang et al., 2009). Consequently, a simultaneous peak in both
350 *Pinus* pollen and fern spores is incompatible with a scenario of solely strengthened, dry winter winds. Instead, this combined
351 signal robustly indicates a cool and humid climatic regime. In this regime, a vigorous EASM delivered high rainfall, which
352 promoted fern-rich vegetation and riverine spore transport, while the EAWM remained active enough to distribute *Pinus* pollen
353 without dominating the climatic regime. Therefore, we propose a possible interpretation for the low *Pinus* during the glacial
354 period and high *Pinus* during the interglacial period: during the glacial period especially during the LGM, a strong but dry
355 EAWM could efficiently transported *Pinus* pollen from distant montane source areas. However, local arid conditions on the
356 exposed continental shelf limited the growth of conifers near the core site leading to moderate percentages in the record; during
357 the interglacial period especially during the Holocene, despite the increased distance due to sea-level rise, enhanced EASM-
358 driven humidity favoured the expansion of Pine forests in source regions. Concurrently, altered atmospheric and oceanic
359 circulation patterns likely facilitated the long-distance transport of pollen to the deep basin.

360 *Artemisia*, Poaceae and Cyperaceae pollen are the main components of terrestrial herbs observed in the core. *Artemisia* spp. is
361 currently widely distributed in temperate grassland and steppe which is associated with cool, semi-arid conditions (Bandara et
362 al., 2023; Sun et al., 2003). Although Poaceae and Cyperaceae pollen indicate a range of different habitats, high percentages
363 of Poaceae pollen in the sediment are suggestive of grassland vegetation, and a high representation of Cyperaceae pollen can
364 point to wetland environments, though in association with *Artemisia* and Poaceae, it may also form part of dry grassland
365 communities (Sun et al., 2003; Wang et al., 2009).

366 Previous studies have found clear temporal variations in pollen assemblages in the SCS characterized by marked higher pollen
367 concentrations in glacial sediments than in interglacial sediments (Jiwarungrueangkul and Liu, 2021; Sun et al., 2000a; Sun
368 and Luo, 2001; Sun et al., 2003; Zheng and Lei, 1999). On one hand, the large amount of pollen in glacial sediments at the site
369 might be transported by a strengthened northeast winter monsoon from the Asian mainland and Taiwan Island. In contrast,
370 during the last glacial low stand, sea level was 120-150 m lower than today, exposing much of the northern SCS continental

371 shelf and increasing land area by roughly 24×104 km² (Chen et al., 2020; Sun et al., 2000a; Wang et al., 2009). The northern
372 SCS would likely receive substantial pollen and spore amounts via wind or water from the exposed continental shelf which
373 was covered by grassland under the prevailing dry and temperate climate of the time (Luo and Sun, 2005; Sun et al., 2003).
374 This expansion of open, terrestrial herb-dominated vegetation likely occurred on both the exposed shelf and the adjacent
375 continental catchments due to the overall drier glacial climate. Typically, during glacial periods, herbaceous vegetation is
376 predominant in the region, whereas during interglacial periods tree and ferns dominate the terrestrial land mass adjacent to the
377 SCS (Sun et al., 2000a; Sun and Luo, 2001). Such glacial-interglacial transitions are driven by changes in climate, or ocean
378 currents, or both. During MIS 2 (21-11.5 ka), *Artemisia* increased again and occupied most of the extensive emerged
379 continental shelf (Sun et al., 2003). Accordingly, the ratio of trees/herbs pollen is a valuable indicator of glacial-interglacial
380 cycles along with their associated vegetation and climate conditions.

381 5.1.3 Dinocysts

382 Although modern dinocyst distributions are strongly correlated with sea surface conditions such as sea surface temperature,
383 sea surface salinity, nutrient levels and productivity (Dale, 1996; Marret and Zonneveld, 2003; Zonneveld et al., 2024),
384 dinocyst deposition and preservation in marine sediments are affected by various non-ecological, taphonomic factors which
385 may alter the primary dinocyst accumulation in the sediment (Holzwarth et al., 2007). It is therefore crucial to account for
386 these factors before relating the fossil dinocyst record to palaeoenvironmental conditions. Upwelling off west Luzon is driven
387 by the EAWM and intensifies during stronger EAWM phases. This process brings nutrient-rich subsurface waters to the surface,
388 promoting enhanced dinoflagellate production (Yuan et al., 2004). The Kuroshio Current, which transports warm and high-
389 salinity water into the northern SCS leading to a significant increase in sea surface temperature, is also a significant factor
390 influencing dinoflagellate growth. Additionally, heterotrophic taxa, such as degradation-sensitive species from the
391 *Protoperidinium* genus, are more susceptible to aerobic degradation compared to autotrophic taxa (Holzwarth et al., 2007).
392 This may be influenced by the water oxygen content which may therefore alter dinocyst assemblages before and after
393 sedimentation (Zonneveld et al., 2008). However, the persistent dominance of heterotrophic dinocysts in the record (up to 99%
394 with mean values of 85%) suggests that selective dissolution of protoperidiniacean species relative to other taxa in the
395 sediments is negligible (Zhao et al., 2017).

396 *Impagidinium* cysts as well as *O. centrocarpum* typically indicate open ocean, fully marine settings characterized by low
397 primary productivity, low nutrient levels, and well-oxygenated bottom waters (Zonneveld et al., 2013; Zonneveld and
398 Pospelova, 2015). Modern surface dinocyst distribution in SCS shows that most of *Impagidinium* species, *Nematosphaeropsis*
399 *labyrinthus* and *Polysphaeridium zoharyi* are positively correlated with water depth. Their highest abundances were observed
400 in the northern slope-deep basin which is influenced by the Kuroshio Current, indicating an open-ocean environment (Li et al.,
401 2020). In the northern Philippine Sea, the predominance of *Impagidinium* taxa from the bottom sediments is also indicative of
402 pelagic and tropical regions (Matsuoka, 1981). During winter, the Kuroshio Current transports high-salinity, low-nutrient
403 waters from the Philippine Sea through the Luzon Strait, which then flows along the continental shelf break, reaching the study
404 area in the northern SCS. This provides further evidence that the increased abundance of Group 1 taxa may reflect typical
405 nutrient-poor open ocean environments and enhanced influence of the Kuroshio Current. Dinocysts preserved in SCS GC-1
406 are dominated by *Brigantedinium* spp. (28-96%, mean = 80%), which have also been observed from sediment trap samples in
407 the southwest Taiwan waters of the SCS with high representation ranging from 68% to 91% (Li et al., 2018b). High abundances
408 of *Brigantedinium* spp. are characteristic of increased nutrient supply (Dale, 1996), which has been used as an indicator of
409 primary productivity (Li et al., 2020; Zonneveld et al., 2013). In addition, *Brigantedinium* spp. is usually more abundant near
410 the winter upwelling zone in the South China Sea (Li et al., 2020). Therefore, Group 2 taxa, characterized by the dominance
411 of *Brigantedinium* spp., indicates intensified upwelling conditions with strong terrigenous influence that contrasts with open-
412 ocean oligotrophic conditions indicated by Group 1. The stratigraphic variation of Group 2 cysts (Fig. 6h) displays an inverse
413 relationship with Mg/Ca-SST, supporting the glacial 'high-productivity/low-temperature' paradigm. Group 3 taxa,
414 characterized by dinocysts such as *Echinidinium* spp. and *S. quanta* are typically adapted to fully marine, eutrophic, and highly
415 productive regimes, and are likely indicative of water column stratification and upwelling processes in open ocean
416 environments (Zonneveld et al., 2013). The shift from Group 2 to Group 3 dominance during the deglaciation may thus signal
417 a transition from terrestrial nutrient-driven productivity to a more stratified, marine-dominated productivity regime.

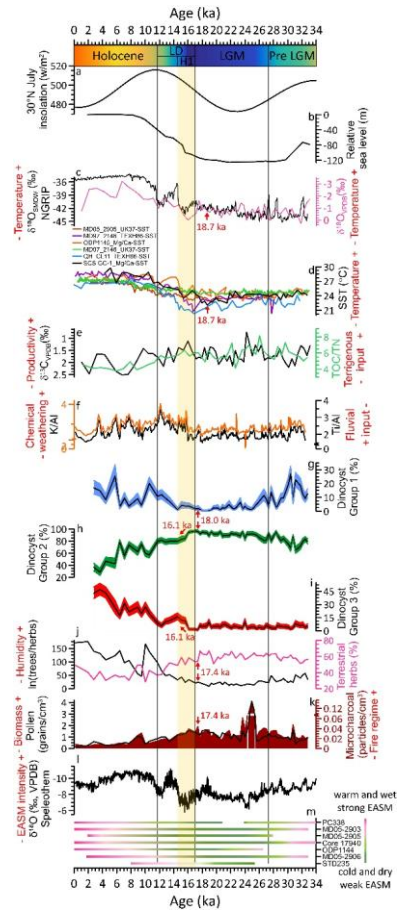
418 5.2 Shelf exposure, aridity and high marine productivity during the LGM

419 Over the past 33 ka, five CONISS-derived statistical zones are grouped into four distinct climatic phases (Fig. 6): pre-LGM
420 (Zone 1, 32.8-27.3 ka), LGM (Zone 2, 27.3-17.0 ka), last deglaciation (Zones 3 and 4, 17.0-11.7 ka), and Holocene (Zone 5,
421 11.7 ka-present) (Figs. 4 and 6). This sequence reveals a pronounced glacial-interglacial transition. The pre-LGM phase
422 relatively already exhibited features of a cooler and drier glacial regime during 32.8-27.3 ka was defined as pre-LGM. The
423 climatic condition, which became more pronounced during the LGM 27.3-17.0 ka, which was characterized by markedly
424 higher sedimentation rates (Fig. 3a), cooler SST (by ca. 3.3°C on average, Figs. 6c and 6d), higher primary productivity (Figs.
425 6e and 6h), reduced humidity (Figs. 6f, 6j, 6l and 6m), a landscape dominated by herbaceous vegetation (Fig. 6j), and
426 strengthened fire activity (Fig. 6k). We refer this interval to the LGM representing the regional expression of glacial conditions
427 in the northern SCS, which is longer than the globally defined LGM (26.5-19.0 ka) (Clark et al., 2009), but consistent with
428 other marine records from the western Pacific marginal seas (Sun et al., 2000a; Wang et al., 2009). Over the past 33 ka, four
429 distinct climatic phases have been clearly recognized based on our multi-proxy record (Fig. 6): pre-LGM (32.8-27.3 ka), LGM
430 (27.3-17.0 ka), last deglaciation (17.0-11.7 ka) which includes the Heinrich Stadial 1 (H1, 17.0-14.5 ka), and the Holocene
431 (11.7 ka-present). This sequence reveals a pronounced glacial-interglacial transition. The pre-LGM phase already exhibited
432 features of a cooler and drier glacial regime, which became more pronounced during the LGM. This period was characterized
433 by markedly higher sedimentation rates (Fig. 3a), cooler SST (Figs. 6c and 6d), higher primary productivity (Figs. 6e and 6h),
434 reduced humidity (Figs. 6f, 6j, 6l and 6m), a landscape dominated by herbaceous vegetation (Fig. 6j), and strengthened fire
435 activity (Fig. 6k).

436 During the LGM, sea levels were approximately 120 m lower than present, leading to extensive exposure of the northern SCS
437 continental shelf (Fig. 6b), which effectively extended the coastal plains and created an expansive, low-relief terrestrial surface
438 (Hanebuth et al., 2000). While previous studies have attributed elevated charcoal and pollen concentrations during the LGM
439 to the reduced distance to sediment sources from this exposed continental shelf (Luo and Sun, 2005; Sun et al., 2000a), our
440 multi-proxy data support this proximal-source effect and further demonstrate that the vegetation colonizing the shelf was
441 fundamentally shaped by the cold and dry glacial climate. Specifically, the high percentages of terrestrial herb pollen, in
442 particular arid-tolerant *Artemisia* together with Poaceae and Cyperaceae, minimum tree pollen (Fig. S2), and trees/herbs ratio
443 (Fig. 6j) all indicate a herbaceous landscape. Moreover, independent climate proxies also confirm the arid conditions: the low
444 K/Al ratio (Fig. 6f) suggesting reduced chemical weathering under drier conditions, aligns with the enriched speleothem $\delta^{18}\text{O}$
445 values indicating a weakened EASM and reduced rainfall over the region (Fig. 6l) (Cheng et al., 2016). This aridity suppressed
446 forest growth and favoured drought-tolerant herbs. Concurrently, the maximal concentrations of microcharcoal (Fig. 6k),
447 especially the large charcoal particles (>100 μm) indicative of local fires (Fig. S6), coincide with maximal herb pollen. This is
448 ecologically explainable: herbaceous vegetation especially in dry seasonal climate could produce fine, highly flammable fuel
449 that supports frequent and potentially high-intensity fires (Zanzarini et al., 2022). Therefore, the high terrestrial herb pollen
450 percentage reflects a dual control: the exposed shelf provided a vast proximal source area, while the glacial climate determined
451 that this area and possibly the adjacent continental catchments would be occupied by drought-adapted grassland/steppe
452 vegetation.

453 The substantially shortened distance between the exposed shelf and the core site (Lambeck et al., 2014) would have facilitated
454 more efficient transfer of terrigenous nutrients to proximal deep-sea areas. The low Ti/Al ratios (Fig. 6f) suggest that this
455 enhanced input originated mainly from felsic continental rivers (e.g., the Pearl River). Although weakened EASM would
456 typically suppress fluvial discharge, this effect appears to have been offset by the closer coastline and the likely persistence of
457 eolian dust transport from the arid Chinese mainland. Concurrently, this open landscape, combined with likely enhanced
458 erosion under such variable glacial conditions would have supplied abundant terrestrial nutrients to the adjacent ocean.
459 Enhanced terrigenous nutrient delivery from this expansive, herb-covered continental shelf and arid continental hinterlands
460 also appears to have stimulated elevated marine productivity during the LGM. This is clearly recorded in our marine proxies:
461 TOC/TN ratio with a range between 3.8-8.1 throughout the record indicates a marine phytoplankton-dominated organic matter
462 source (Meyers, 1999), while elevated $\delta^{13}\text{C}$ values of planktonic foraminifera (Fig. 6e) during this period suggest enhanced
463 organic carbon export. Critically, the combined fluvial and eolian nutrient fluxes would have created a nutrient-replete surface
464 ocean, directly favouring heterotrophic dinoflagellates such as *Brigantedinium* (Smayda and Trainer, 2010). This can thereby
465 well explain the dinocyst record characterized by pronounced dominance of dinocyst Group 2 (*Brigantedinium* spp. which can

466 constitute up to 97%, mean = 81%) indicative of high nutrient availability, alongside the near-absence of oligotrophic, open-
 467 ocean Group 1 (Figs. 6g and 6h), points to a productivity regime sustained by abundant terrestrial nutrient supply rather than
 468 open-ocean processes. This pattern is consistent with global compilations showing that organic carbon accumulation rates
 469 during glacial maxima were ~50% higher than interglacial intervals (Cartapanis et al., 2016). Independent evidence from the
 470 northern SCS similarly links higher glacial productivity to intensified winter monsoon winds, enhanced water-column mixing,
 471 upwelling, and increased land-derived nutrient supply (Li et al., 2008). Our dinocyst record, characterized by the dominance
 472 of a heterotrophic, highly nutrient-dependent taxon, strongly supports the interpretation that terrestrial nutrient supply was a
 473 key mechanism together with the complementation of the physical forcing of strengthened winter monsoon-driven mixing.



474

475 **Figure 6:** 30°N July insolation (Laskar et al., 2004) (a); relative sea level on the Sunda Shelf, **South-China-Sea** (Hanebuth et
476 al., 2000) (b); NGRIP $\delta^{18}\text{O}_{\text{SMOW}}$ (Andersen et al., 2004) (c, black) and stable oxygen $\delta^{18}\text{O}_{\text{VPDB}}$ of planktonic foraminifera from
477 SCS GC-1 (c, pink); SST records from MD052905 (Zhou et al., 2012), MD972146 (Lin et al., 2014), ODP1145 (Oppo and
478 Sun, 2005), QHCL11 (Liu et al., 2020) and SCS GC-1 (d); stable carbon $\delta^{13}\text{C}_{\text{VPDB}}$ of planktonic foraminifera (e, black) and
479 TOC/TN ratio (e, green); major element ratio Ti/Al (f, black) and K/Al (f, orange), percentages of three dinocyst groups (g, h,
480 i); ratio of trees/herbs (j, black) and percentages of terrestrial herbs (j, pink); pollen concentration (k, black) and microcharcoal
481 concentration (k, dark red shading); compilation of speleothem $\delta^{18}\text{O}_{\text{VPDB}}$ values from central China (l) (Cheng et al., 2016);
482 summary of records indicating climate and potential intensity of EASM (m) (Sun et al., 2000a; Sun et al., 2000b; Luo and Sun,
483 2005; Zhou et al., 2012; Xie et al., 2014; Dai and Weng, 2015; Dai et al., 2015a; Yu et al., 2017; Li et al., 2019). Pre LGM:
484 pre Last Glacial Maximum; LGM: Last Glacial Maximum; LD: last deglaciation; H1: Heinrich Stadial 1. Red arrows indicate
485 the onset of the transition in different proxies.

486 5.3 Early ocean warming, monsoon intensification and ecosystem response since the last deglaciation

487 Since the last deglaciation, the northern SCS has experienced a comprehensive environmental transformation characterized by
488 decreasing sedimentation rates, rising SST, declining primary productivity, increased moisture availability, a pronounced
489 expansion of pine forests, and reduced fire activity. Critically, our record reveals that the initial signal of this transformation
490 was an SST increase at ca. 18.7 ka (Figs. 6c and 6d) (Andersen et al., 2004; Lin et al., 2014; Liu et al., 2020; Oppo and Sun,
491 2005; Zhou et al., 2012), which began ~1.3 ka earlier than the major shifts in terrestrial vegetation and other sediment proxies
492 (ca. 17.4 ka, Figs. 6j and 6k). This early ocean warming provides direct, local evidence for the primacy of ocean-atmosphere
493 forcing in initiating the regional deglacial transition. Additionally, the millennial-scale event of H1 (17.0-14.5 ka) is embedded
494 within the early phase of this warming, recorded as an interval of low SST, high $\delta^{18}\text{O}_{\text{VPDB}}$ of planktonic foraminifera and high
495 percentages of terrestrial herb pollen. This interval interpreted as the regional expression of H1 in the northern SCS, falls
496 within the broader range of published H1 chronologies (17.5-14.5 ka, Denton et al., 2006; 18-15.6 ka, Sánchez Goñi and
497 Harrison, 2010) and is consistent with other western Pacific records (Xu et al., 2013). This suggests that short-period cold and
498 dry conditions linked to North Atlantic forcing temporarily modulated but did not override the underlying tropical warming
499 trend in the study area (Clark et al., 2012). However, the Bolling-Allerød (B-A, 14.5–12.9 ka) and Younger Dryas (YD, 12.9–
500 11.7 ka) are not clearly identified in our proxies. Instead, our record shows a progressive trend toward warmer, wetter, and
501 more forested conditions from 14.5 ka onward, without distinct reversals or plateaus.

502 The earlier onset of SST warming corresponds more closely with rising boreal summer insolation (Fig. 6a) (Laskar et al., 2004)
503 than with the rate of sea-level rise (Fig. 6b) (Hanebuth et al., 2000). This implies that tropical ocean warming, likely amplified
504 by ocean-atmosphere feedbacks, acted as the initial trigger for subsequent environmental changes. This effect is especially
505 pronounced in the tropics and is consistent with the concept of tropical ocean-atmosphere forcing (Cheng et al., 2019; Xie et
506 al., 2010). For instance, seminal work has shown that the timing of peak East Asian Monsoon intensity differs between marine
507 and terrestrial records (An et al., 2000). Furthermore, while terrestrial pollen records from East Asian indicate rapid warming
508 around 15 ka, synchronous with Greenland ice core and stalagmite records from southern China, marine SST reconstructions
509 (based on Mg/Ca-SST and long chain alkenone U^{37} -SST) from the same record indicate that SSTs began to rise as early as
510 20-19 ka, a trend more consistent with the early warming of the Western Pacific Warm Pool (Xu et al., 2013). This 3-4 kyr lag
511 of terrestrial warming behind western Pacific oceanic warming highlights the differential thermal response and reinforces the
512 interpretation that early ocean warming served as a critical forcing mechanism.

513 The sequence of multi-proxy changes in our record reveals a clear mechanistic chain initiated by this early SST rise. The first
514 detectable response in our marine proxies is a shift in dinocyst assemblages at ca. 18.0 ka, marked by the incipient increase of
515 oligotrophic Group 1 dinocysts and the onset of decline in the highly nutrient-dependent Group 2 dinocysts. We attribute this
516 to a direct oceanographic response to warming: enhanced upper water column stratification reduced vertical nutrient supply,
517 favoring oligotrophic taxa over heterotrophic ones. Subsequent to this initial marine response, the physical reconfiguration of
518 the coastline due to sea level rise further modulated the environmental trajectory. The inundation of the exposed continental
519 shelf increased the distance from terrestrial sediment sources to the core site (Luo and Sun, 2005; Sun et al., 2000a) and created
520 a sediment trap on the newly formed shallow marine environments, leading to a dramatic reduction in terrigenous material
521 reaching our deep basin site (Liu et al., 2003; Wang and Sun, 1994). This is reflected in markedly lower sedimentation rates

Formatted: Font: Not Bold

Formatted: Font: (Default)+Body (Times New Roman), 10 pt, Not Highlight

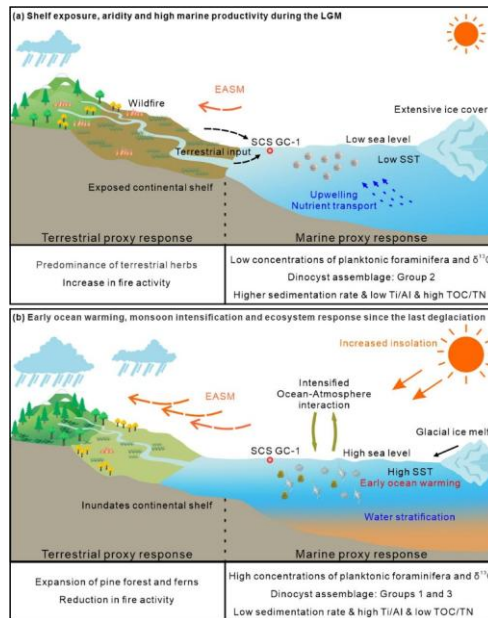
Formatted: Font: (Default)+Body (Times New Roman), 10 pt, Not Highlight

522 and increased Ti/Al ratios (Figs. 3a and 6f), indicating reduced terrestrial input. The combination of sustained ocean warming
523 and reduced nutrient supply further suppressed heterotrophic dinoflagellates such as *Brigantedinium* (Smayda and Trainer,
524 2010), driving a pronounced decline in Group 2 dinocysts from 16.1 ka and a concurrent increase in Group 3 dinocysts which
525 is indicative of more stratified, marine-dominated conditions (Figs. 6h and 6i), coincident with a reduction in TOC/TN (Fig.
526 6e). This shift marks a fundamental transition in the productivity regime: from a terrigenous nutrient-driven regime (Group 2
527 dominated during the LGM) to a more stratified, marine-dominated regime (Group 3).

528 Parallel to these oceanic changes, the shrinking continental shelf also constrained the habitat for herbaceous vegetation.
529 Concurrently, the intensification of the EASM, a large-scale atmospheric response like initiated and reinforced by the warming
530 tropical ocean and the evolving land-sea thermal contrast, is recorded by the rapid negative shift in the speleothem $\delta^{18}\text{O}$ records
531 (Fig. 6l) (Cheng et al., 2016) and supported by multiple palaeorecords from the northern SCS (Fig. 6m) (Dai and Weng, 2015;
532 Dai et al., 2015; Li et al., 2019; Luo et al., 2015; Sun et al., 2000a; Sun et al., 2000b; Xie et al., 2014; Yu et al., 2017; Zhou et al.,
533 2012). This strengthened monsoon brought increased moisture to the region, supporting the expansion of pine forests and
534 ferns (Figs. 4 and 6j) and leading to a sharp reduction in fire activity, as evidenced by decreased charcoal concentrations (Fig.
535 6k).

536 Additional evidence supports this ecosystem-scale reorganization. Relatively high concentrations of foraminiferal organic
537 linings (Fig. 4) indicate that water depth and open ocean environments had become suitable for planktonic foraminifera
538 (Tyszka et al., 2021), while the decline in coprophilous fungal spores suggests an ecosystem-level response in herbivore
539 populations to the changing landscape (Fig. 4) (Lee et al., 2022). Similar patterns with increased fern spores, decreased
540 terrestrial herbs and reduced dinocyst concentrations were also recorded from 12.5-6.8 ka in the core GLW31D from the
541 northern SCS (Li et al., 2017). Additionally, periodic peaks in oligotrophic, open-ocean dinocyst Group 1, particularly around
542 10.6 ka and 5.8 ka (Fig. 6g), point to short enhancements of the warm, nutrient-poor Kuroshio Current intrusion (Liu et al.,
543 2016b), which would further suppressed productivity in the northern SCS. Independent evidence for strengthened Kuroshio
544 intrusion during the early Holocene is also recorded in core GLW31D from the northern SCS (Li et al., 2021).

545 Collectively, our multi-proxy dataset demonstrates that the deglacial environmental transition in the northern SCS reflects the
546 complex interplay of multiple forcings (Fig. 7). The sequence began with tropical ocean warming, evidenced by the early rise
547 in SST, which initiated the deglacial transition. This warming directly altered marine conditions (stratification, productivity)
548 and, throughout ocean-atmospheric interactions, helped trigger the intensification of the EASM. These primary changes were
549 then amplified and modulated by the physical effects of sea-level rise (altered sediment transport and coastal geography). This
550 multi-mechanism framework highlights the northern SCS as a sensitive region where the coherent yet time-transgressive
551 responses of marine and terrestrial systems to global climatic changes are clearly recorded during the last deglaciation.



552

553 **Figure 7:** A conceptual framework of driving mechanisms and associated environmental responses during the LGM (a) and
554 since the last deglaciation (b) based on multi-proxy record from the core SCS GC-1 in the northern SCS.

555 6 Conclusions

556 Our multi-proxy reconstruction from the northern SCS provides a high-resolution record of clear glacial-interglacial climatic
557 and oceanic transitions over the past 33 ka. Four distinct climatic phases are identified, viz. the pre-Last Glacial Maximum
558 (32.8-27.3 ka), Last Glacial Maximum (27.3-17.0 ka), last deglaciation (including the Heinrich Stadial 1) (17.0-11.7 ka) and
559 the Holocene (11.7 ka-present). The glacial intervals (pre-LGM and LGM) were characterized by higher sedimentation rates,
560 cooler SST, higher primary productivity, herb-dominated landscapes, reduced humidity and intensified fire activity. This
561 regime was primarily shaped by the effects of glacial low sea-level stand and arid climatic conditions, which together promoted
562 the expansion of open vegetation and enhanced the supply of terrestrial nutrients, thereby stimulating marine productivity. A
563 fundamental regime shift occurred during the last deglaciation, marked by evidently decreasing sedimentation rates, rising
564 SST, declining primary productivity, a pronounced expansion of pine forests, increased moisture availability, and diminished
565 fire activity. The early onset of SST warming (1.3 ka ahead of terrestrial shifts), points to tropical ocean-atmospheric
566 interactions as the initial trigger for the deglacial transition. The Holocene was characterized by a period of relative stability,
567 defined by the lowest sedimentation rates, warmest SST, highest humidity, maximum pine forest coverage and minimal fire
568 disturbance. In summary, the combined evidence reveals that the environmental changes of the northern SCS since the last
569 glacial period reflects a shift in the dominant climate forcing mechanisms. During the glacial period, the system was governed
570 by the combined forcing of low sea level and continental aridity, which amplified land-sea interactions and maintained high
571 marine productivity. Since the last deglaciation, the climate dynamics have transitioned to a regime where low-latitude

572 processes, initiated by early ocean warming and subsequent ocean-atmosphere coupling, became the primary driver, leading
573 to monsoon intensification and thereafter ecosystem reorganization. This study highlights the value of integrated land-sea
574 proxies in deciphering complex climate interactions and underscores the northern SCS's sensitivity to both high- and low-
575 latitude forcing. Future research employing a spatial network of cores across the SCS will be crucial to better resolve the spatial
576 patterns and teleconnections of these changes.

577 **Author Contributions**

578 Xueqin Zhao: Conceptualization, Data curation, Formal analysis, Funding acquisition, Investigation, Methodology, Project
579 administration, Supervision, Validation, Writing – original draft, Writing – review and editing; Shengjie Ye: Investigation,
580 Visualization, Writing – review and editing; Jiahui Yao: Investigation, Formal analysis, Writing – review and editing; Michael
581 Meadows: Validation, Writing – review and editing; Chengyu Weng: Validation, Writing – review and editing; Yasong Wang:
582 Visualization, Writing – review and editing; Mingxing Zhang: Investigation; Yunping Xu: Conceptualization, Writing – review
583 and editing.

584 **Competing Interests**

585 The authors declare that they have no conflict of interest.

586 **Acknowledgments**

587 This work was supported by the National Natural Science Foundation of China (42206048). We would like to thank the captain,
588 crew and especially all scientists of the R/V Songhang (Shanghai Ocean University) cruise for recovering the samples. Thank
589 Xiaodi Lu and Yinwei Xi for the sampling and helping to measure XRF. Thank Xiaodi Lu for the assistance with lab analysis.
590 Mike E. Meadows acknowledges financial support from the Jiangsu Provincial Government Overseas Talent 100 Plan,
591 SBX2021010183. [We thank the three anonymous reviewers for their useful and constructive comments that have helped to](#)
592 [improve the manuscript.](#)

593 **Data Availability**

594 Data used in this study has been stored in the Pangaea database (<https://www.pangaea.de>) with specific DOI:
595 <https://doi.pangaea.de/10.1594/PANGAEA.987882> for pollen and spore , <https://doi.pangaea.de/10.1594/PANGAEA.987861>
596 for organic-walled dinoflagellate cyst, <https://doi.pangaea.de/10.1594/PANGAEA.987870> for microcharcoal,
597 <https://doi.pangaea.de/10.1594/PANGAEA.989845> for organic carbon and nitrogen content,
598 <https://doi.pangaea.de/10.1594/PANGAEA.989928> for foraminifera stable carbon and oxygen isotopes, and
599 <https://doi.pangaea.de/10.1594/PANGAEA.989846> for X-ray fluorescence (XRF) scanning data.

600 **References**

601 Aleman, J. C., Blarquez, O., Bentaleb, I., Bonté, P., Brossier, B., Carcaillet, C., Gond, V., Gourlet - Fleury, S., Kpolita, A.,
602 Lefèvre, I., Oslisly, R., Power, M. J., Yongo, O. D., Bremond, L., and Favier, C.: Tracking land-cover changes with
603 sedimentary charcoal in the Afrotropics. *Holocene*, 23, 1853-1862, doi: 10.1177/0959683613508159, 2013.
604 An, Z.: The history and variability of the East Asian paleomonsoon climate. *Quat. Sci. Rev.*, 19(1), 171-187, doi: S0277-
605 3791(99)00060-8, 2000.

606 An, Z., Porter, S. C., Kutzbach, J. E., Xihao, W., Suming, W., Xiaodong, L., Xiaoqiang, L., and Weijian, Z.: Asynchronous
607 Holocene optimum of the East Asian monsoon. *Quat. Sci. Rev.*, 19(8), 743-762, doi: 10.1016/S0277-3791(99)00031-1,
608 2000.

609 Andersen, K. K., Azuma, N., Barnola, J. M., Bigler, M., Biscaye, P., Caillon, N., Chappellaz, J., Clausen, H. B., Dahl-Jensen,
610 D., Fischer, H., Flückiger, J., Fritzsche, D., Fujii, Y., Goto-Azuma, K., Grønbold, K., Gundestrup, N. S., Hansson, M.,
611 Huber, C., Hvidberg, C. S., Johnsen, S. J., Jonsell, U., Jouzel, J., Kipfstuhl, S., Landais, A., Leuenberger, M., Lorrain, R.,
612 Masson-Delmotte, V., Miller, H., Motoyama, H., Narita, H., Popp, T., Rasmussen, S. O., Raynaud, D., Rothlisberger, R.,
613 Ruth, U., Samyn, D., Schwander, J., Shoji, H., Siggard-Andersen, M. L., Steffensen, J. P., Stocker, T., Sveinbjörnsdóttir,
614 A. E., Svensson, A., Takata, M., Tison, J. L., Thorsteinsson, T., Watanabe, O., Wilhelms, F., White, J. W. C., and North
615 Greenland Ice Core Project, m.: High-resolution record of Northern Hemisphere climate extending into the last
616 interglacial period. *Nature*, 431(7005), 147-151, doi: 10.1038/nature02805, 2004.

617 Bandara, G., Luo, C. X., Chen, C. X., Xiang, R., Herath, D. B., Yang, Z. J., and Thilakanayaka, V.: Sedimental pollen records
618 in the northern South China Sea and their paleoenvironmental significance. *J. Asian Earth Sci.*, 241, Article 105457, doi:
619 10.1016/j.jseas.2022.105457, 2023.

620 Barker, S., Greaves, M., and Elderfield, H.: A study of cleaning procedures used for foraminiferal Mg/Ca paleothermometry.
621 *Geochem. Geophys. Geosyst.*, 4(9), doi: 10.1029/2003GC000559, 2003.

622 Blaauw, M., and Christen, J. A.: Flexible paleoclimate age-depth models using an autoregressive gamma process. *Bayesian*
623 *Anal.*, 6(3), 457-474, 418, doi: 10.1214/11-BA618, 2011.

624 Cartapanis, O., Bianchi, D., Jaccard, S. L., and Galbraith, E. D.: Global pulses of organic carbon burial in deep-sea sediments
625 during glacial maxima. *Nat. Commun.*, 7(1), 10796, doi: 10.1038/ncomms10796, 2016.

626 Chao, S., Shaw, P., and Wang, J.: Wind relaxation as possible cause of the South China Sea Warm Current. *J. Oceanogr.*,
627 51(1), 111-132, doi: 10.1007/BF02235940, 1995.

628 Chen, C. A., and Huang, M.: A mid-depth front separating the South China Sea water and the Philippine sea water. *J. Oceanogr.*,
629 52(1), 17-25, doi: 10.1007/BF02236530, 1996.

630 Cheng, H., Edwards, R. L., Sinha, A., Spötl, C., Yi, L., Chen, S., Kelly, M., Kathayat, G., Wang, X., Li, X., Kong, X., Wang,
631 Y., Ning, Y., and Zhang, H.: The Asian monsoon over the past 640,000 years and ice age terminations. *Nature*, 534(7609),
632 640-646, doi: 10.1038/nature18591, 2016.

633 Chen, Y., Huang, E., Schefuß, E., Mohtadi, M., Steinke, S., Liu, J., Martínez-Méndez, G., and Tian, J.: Wetland expansion on
634 the continental shelf of the northern South China Sea during deglacial sea level rise. *Quat. Sci. Rev.*, 231, 106202, doi:
635 10.1016/j.quascirev.2020.106202, 2020.

636 Cheng, L., Abraham, J., Hausfather, Z., and Trenberth, K. E.: How fast are the oceans warming? *Science*, 363(6423), 128-129,
637 doi: 10.1126/science.aav7619, 2019.

638 Cheng, Z., Wu, J., Luo, C., Liu, Z., Huang, E., Zhao, H., Dai, L., and Weng, C.: Coexistence of savanna and rainforest on the
639 ice-age Sunda Shelf revealed by pollen records from southern South China Sea. *Quat. Sci. Rev.*, 301, 107947, doi:
640 10.1016/j.quascirev.2022.107947, 2023.

641 Clark, P. U., Shakun, J. D., Baker, P. A., Bartlein, P. J., Brewer, S., Brook, E., Carlson, A. E., Cheng, H., Kaufman, D. S., Liu,
642 Z., Marchitto, T. M., Mix, A. C., Morrill, C., Otto-Bliesner, B. L., Pahnke, K., Russell, J. M., Whitlock, C., Adkins, J. F.,
643 Blois, J. L., Clark, J., Colman, S. M., Curry, W. B., Flower, B. P., He, F., Johnson, T. C., Lynch-Stieglitz, J., Markgraf,
644 V., McManus, J., Mitrovica, J. X., Moreno, P. I., and Williams, J. W.: Global climate evolution during the last deglaciation.
645 *Proc. Natl. Acad. Sci. U. S. A.*, 109(19), E1134-E1142, doi:10.1073/pnas.1116619109, 2012. Clift, P. D., Hodges, K. V.,
646 Heslop, D., Hannigan, R., Van Long, H., and Calves, G.: Correlation of Himalayan exhumation rates and Asian monsoon
647 intensity. *Nat. Geosci.*, 1(12), 875-880, doi: 10.1038/ngeo351, 2008.

648 Conedera, M., Tinner, W., Neff, C., Meurer, M., Dickens, A. F., and Krebs, P.: Reconstructing past fire regimes: methods,
649 applications, and relevance to fire management and conservation. *Quat. Sci. Rev.*, 28(5), 555-576, doi:
650 10.1016/j.quascirev.2008.11.005, 2009.

651 Dai, L., and Weng, C.: A survey on pollen dispersal in the western Pacific Ocean and its paleoclimatological significance as a
652 proxy for variation of the Asian winter monsoon. *Sci. China Earth Sci.*, 54(2), 249-258, doi: 10.1007/s11430-010-4027-
653 7, 2011.

654 Dai, L., and Weng, C.: Marine palynological record for tropical climate variations since the late last glacial maximum in the
655 northern South China Sea. *Deep-Sea. Res. Pt II*, 122, 153-162, doi: 10.1016/j.dsr2.2015.06.011, 2015.

656 Dai, L., Weng, C., and Mao, L.: Patterns of vegetation and climate change in the northern South China Sea during the last
657 glaciation inferred from marine palynological records. *Palaeogeogr., Palaeoclimatol., Palaeoecol.*, 440, 249-258, doi:
658 10.1016/j.palaeo.2015.08.041, 2015.

659 Dale, B.: Dinoflagellate cyst ecology: modeling and geological applications. In J. Jansonius and D. C. McGregor (Eds.),
660 *Palynology: principles and applications* (Vol. 3, pp. 1249-1275). American Association of Stratigraphic Palynologists
661 Foundation, 1996.

662 [Denton, G., Broecker, W., and Alley, R.: The mystery interval 17.5 to 14.5 kyrs ago. *PAGES news*, 14\(2\), 14-16. doi:
663 10.22498/pages.14.2.14, 2006.](#)

664 Ding, Z., Yu, Z., Rutter, N. W., and Liu, T.: Towards an orbital time scale for chinese loess deposits. *Quat. Sci. Rev.*, 13(1),
665 39-70, doi: 10.1016/0277-3791(94)90124-4, 1994.

666 Fang, G., Fang, W. D., and Wang, K.: A survey of the study of the South China Sea upper ocean circulation. *Acta Oceanog.*
667 *Tai.*, 37, 1-16, 1998.

668 Felden, J., Möller, L., Schindler, U., Huber, R., Schumacher, S., Koppe, R., Diepenbroek, M., and Glöckner, F. O.: PANGAEA
669 – Data Publisher for Earth & Environmental Science. *Sci. Data*, 10(1), 347, doi: 10.1038/s41597-023-02269-x, 2023.

670 Govin, A., Holzwarth, U., Heslop, D., Ford Keeling, L., Zabel, M., Mulitza, S., Collins, J. A., and Chiessi, C. M.: Distribution
671 of major elements in Atlantic surface sediments (36°N–49°S): Imprint of terrigenous input and continental weathering.
672 *Geochem. Geophys. Geosyst.*, 13(1), doi: 10.1029/2011GC003785, 2012.

673 Grimm, E.: Tilia and TGVView 19 version 2.0. 41. software. Springfield, USA: Illinois State Museum, Research and Collection
674 Center, 2015.

675 Hanebuth, T., Statterger, K., and Grootes, P. M.: Rapid flooding of the Sunda Shelf: A late-glacial sea-level record. *Science*,
676 288(5468), 1033-1035, doi: 10.1126/science.288.5468.1033, 2000.

677 Haynes, J. R.: *Foraminifera*. Palgrave Macmillan London, doi: 10.1007/978-1-349-05397-1, 1981.

678 Holzwarth, U., Esper, O., and Zonneveld, K.: Distribution of organic-walled dinoflagellate cysts in shelf surface sediments of
679 the Benguela upwelling system in relationship to environmental conditions. *Mar. Micropaleontol.*, 64(1–2), 91-119, doi:
680 10.1016/j.marmicro.2007.04.001, 2007.

681 Hu, D., Clift, P. D., Böning, P., Hannigan, R., Hillier, S., Blusztajn, J., Wan, S., and Fuller, D. Q.: Holocene evolution in
682 weathering and erosion patterns in the Pearl River delta. *Geochem. Geophys. Geosyst.*, 14(7), 2349-2368, doi:
683 10.1002/ggge.20166, 2013.

684 Hu, J., Kawamura, H., Hong, H., and Qi, Y.: A review on the currents in the South China Sea: Seasonal circulation, South
685 China Sea warm current and Kuroshio intrusion. *J. Oceanogr.*, 56(6), 607-624, doi: 10.1023/A:1011117531252, 2000.

686 Huang, C., Wu, L., Cheng, J., Qu, X., Luo, Y., Zhang, H., Ye, F., and Wei, G.: Sedimentary responses to climatic variations
687 and Kuroshio intrusion into the northern South China Sea since the last deglaciation. *Global Planet. Change*, 245, 104671,
688 doi: 10.1016/j.gloplacha.2024.104671, 2025.

689 Huang, K., You, C., Lin, H., and Shieh, Y.: In situ calibration of Mg/Ca ratio in planktonic foraminiferal shell using time series
690 sediment trap: A case study of intense dissolution artifact in the South China Sea. *Geochem. Geophys. Geosyst.*, 9(4),
691 doi: 10.1029/2007GC001660, 2008.

692 Hughen, K. A., Baillie, M. G. L., Bard, E., Warren Beck, J., Bertrand, C. J. H., Blackwell, P. G., Buck, C. E., Burr, G. S.,
693 Cutler, K. B., Damon, P. E., Edwards, R. L., Fairbanks, R. G., Friedrich, M., Guilderson, T. P., Kromer, B., McCormac,
694 G., Manning, S., Bronk Ramsey, C., Reimer, P. J., Reimer, R. W., Remmele, S., Southon, J. R., Stuiver, M., Talamo, S.,
695 Taylor, F. W., Van der Plicht, J., and Weyhenmeyer, C. E.: Marine04 marine radiocarbon age calibration, 0–26 cal kyr
696 BP. *Radiocarbon*, 46(3), 1059-1086, doi: 10.1017/S0033822200033002, 2004.

697 Jiwaringrueangkul, T., and Liu, Z.: East Asian monsoon and sea-level controls on clay mineral variations in the southern
698 South China Sea since the Last Glacial Maximum. *Quat. Int.*, 592, 1-11, doi: 10.1016/j.quaint.2021.04.033, 2021.

699 Kaars, S. v. d., Wang, X., Kershaw, P., Guichard, F., and Setiabudi, D. A.: A Late Quaternary palaeoecological record from
700 the Banda Sea, Indonesia: patterns of vegetation, climate and biomass burning in Indonesia and northern Australia.
701 *Palaeogeogr., Palaeoclimatol., Palaeoecol.*, 155(1), 135-153, doi: 10.1016/S0031-0182(99)00098-X, 2000.

702 Kissel, C., Laj, C., Jian, Z., Wang, P., Wandres, C., and Rebolledo-Vieyra, M.: Past environmental and circulation changes in
703 the South China Sea: Input from the magnetic properties of deep-sea sediments. *Quat. Sci. Rev.*, 236, 106263, doi:
704 10.1016/j.quascirev.2020.106263, 2020.

705 Lambeck, K., Rouby, H., Purcell, A., Sun, Y., and Sambridge, M.: Sea level and global ice volumes from the Last Glacial
706 Maximum to the Holocene. *Proc. Natl. Acad. Sci. U. S. A.*, 111(43), 15296-15303, doi: 10.1073/pnas.1411762111, 2014.

707 Laskar, J., Robutel, P., Joutel, F., Gastineau, M., Correia, A. C. M., and Levrard, B.: A long-term numerical solution for the
708 insolation quantities of the Earth. *Astronomy & Astrophysics*, 428, 261-285, doi: 10.1051/0004-6361:20041335, 2004.

709 Lee, C. M., van Geel, B., and Gosling, W. D.: On the use of spores of coprophilous fungi preserved in sediments to indicate
710 past herbivore presence. *Quaternary*, 5(3), 30, doi: 10.3390/quat5030030, 2022.

711 Li, C., Li, Y., Zheng, Y., Yu, S., Tang, L., Li, B., and Cui, Q.: A high-resolution pollen record from East China reveals large
712 climate variability near the Northgrippian-Meghalayan boundary (around 42 years ago) exerted societal influence.
713 *Palaeogeogr., Palaeoclimatol., Palaeoecol.*, 512, 156-165, doi: 10.1016/j.palaeo.2018.07.031, 2018a.

714 Li, L., Wang, H., Luo, B., and He, J.: The characterizations and paleoceanographic significances of organic and inorganic
715 carbon in northern South China Sea during past 40 ka. *Mar. Geol. & Qua. Geol.*, 28(6), 79-85, doi:
716 10.3724/sp.J.1140.2008.06079, 2008.

717 Li, M., Ouyang, T., Tian, C., Zhu, Z., Peng, S., Tang, Z., Qiu, Y., Zhong, H., and Peng, X.: Sedimentary responses to the East
718 Asian monsoon and sea level variations recorded in the northern South China Sea over the past 3 kyr. *J. Asian Earth Sci.*,
719 171, 213-224, doi: 10.1016/j.jseaes.2018.01.001, 2019.

720 Li, Z., Pospelova, V., Kawamura, H., Luo, C., Mertens, K. N., Hernández-Almeida, I., Yin, K., Wu, Y., Wu, H., and Xiang,
721 R.: Dinoflagellate cyst distribution in surface sediments from the South China Sea in relation to hydrographic conditions
722 and primary productivity. *Mar. Micropaleontol.*, 159, 101815, doi: 10.1016/j.marmicro.2019.101815, 2020.

723 Li, Z., Pospelova, V., Lin, H.-L., Liu, L., Song, B., and Gong, W.: Seasonal dinoflagellate cyst production and terrestrial
724 palynomorph deposition in the East Asian Monsoon influenced South China Sea: A sediment trap study from the
725 Southwest Taiwan waters. *Rev. Palaeobot. Palynol.*, 257, 117-139, doi: 10.1016/j.revpalbo.2018.07.007, 2018b.

726 Li, Z., Pospelova, V., Liu, L., Francois, R., Wu, Y., Mertens, K. N., Saito, Y., Zhou, R., Song, B., and Xie, X.: High-resolution
727 reconstructions of Holocene sea-surface conditions from dinoflagellate cyst assemblages in the northern South China Sea.
728 *Mar. Geol.*, 438, 106528, doi: 10.1016/j.margeo.2021.106528, 2021.

729 Li, Z., Pospelova, V., Liu, L., Zhou, R., and Song, B.: High-resolution palynological record of Holocene climatic and
730 oceanographic changes in the northern South China Sea. *Palaeogeogr., Palaeoclimatol., Palaeoecol.*, 483, 94-124, doi:
731 10.1016/j.palaeo.2017.03.009, 2017.

732 Li, Z., Pospelova, V., Mertens, K. N., Liu, L., Wu, Y., Li, C., and Gu, H.: Evaluation of organic-walled dinoflagellate cyst
733 distributions in coastal surface sediments of the China Seas in relation with hydrographic conditions for
734 paleoceanographic reconstruction. *Quat. Int.*, 661, 60-75, doi: 10.1016/j.quaint.2023.03.007, 2023.

735 Lin, D., Chen, M., Yamamoto, M., and Yokoyama, Y.: Millennial-scale alkenone sea surface temperature changes in the
736 northern South China Sea during the past 45,000 years (MD972146). *Quat. Int.*, 333, 207-215, doi:
737 10.1016/j.quaint.2014.03.062, 2014.

738 Liu, J., Xiang, R., Chen, Z., Chen, M., Yan, W., Zhang, L., and Chen, H.: Sources, transport and deposition of surface
739 sediments from the South China Sea. *Deep Sea Res. (I Oceanogr. Res. Pap.)*, 71, 92-102, doi: 10.1016/j.dsr.2012.09.006,
740 2013.

741 Liu, J., Xiang, R., Kao, S. J., Fu, S., and Zhou, L.: Sedimentary responses to sea-level rise and Kuroshio Current intrusion
742 since the Last Glacial Maximum: Grain size and clay mineral evidence from the northern South China Sea slope.
743 *Palaeogeogr., Palaeoclimatol., Palaeoecol.*, 450, 111-121, doi: 10.1016/j.palaeo.2016.03.002, 2016a.

744 Liu, K., Chao, S., Shaw, P., Gong, G., Chen, C., and Tang, T.: Monsoon-forced chlorophyll distribution and primary production
745 in the South China Sea: observations and a numerical study. *Deep Sea Res. (I Oceanogr. Res. Pap.)*, 49(8), 1387-1412,
746 doi: 10.1016/S0967-0637(02)00035-3, 2002.

747 Liu, L., Guan, H., Feng, J., Xu, L., Mao, S., and Liu, L.: Composition of glycerol dibiphytanyl glycerol tetraethers (GDGTs)
748 and its responses to paleotemperature and monsoon changes since 31ka in northern South China Sea. *Mar. Geol. & Qua.*
749 *Geol.*, 40(3), 144-159, doi: 10.16562/j.cnki.0256-1492.2020021101, 2020.

750 Liu, Z., Colin, C., Li, X., Zhao, Y., Tuo, S., Chen, Z., Siringan, F. P., Liu, J. T., Huang, C.-Y., You, C.-F., and Huang, K.-F.:
751 Clay mineral distribution in surface sediments of the northeastern South China Sea and surrounding fluvial drainage
752 basins: Source and transport. *Mar. Geol.*, 277(1), 48-60, doi: 10.1016/j.margeo.2010.08.010, 2010.

753 Liu, Z., Trentesaux, A., Clemens, S. C., Colin, C., Wang, P., Huang, B., and Boulay, S.: Clay mineral assemblages in the
754 northern South China Sea: implications for East Asian monsoon evolution over the past 2 million years. *Mar. Geol.*,
755 201(1), 133-146, doi: 10.1016/S0025-3227(03)00213-5, 2003.

756 Liu, Z., Zhao, Y., Colin, C., Statterger, K., Wiesner, M. G., Huh, C., Zhang, Y., Li, X., Sompongchaiyakul, P., You, C., Huang,
757 C., Liu, J. T., Siringan, F. P., Le, K. P., Sathiamurthy, E., Hantoro, W. S., Liu, J., Tuo, S., Zhao, S., Zhou, S., He, Z.,
758 Wang, Y., Bunsomboonsakul, S., and Li, Y.: Source-to-sink transport processes of fluvial sediments in the South China
759 Sea. *Earth-Sci. Rev.*, 153, 238-273, doi: 10.1016/j.earscirev.2015.08.005, 2016b.

760 Luo, C., Chen, C., Xiang, R., Jiang, W., Liu, J., Lu, J., Su, X., Zhang, Q., Yang, Y., and Yang, M.: Study of modern pollen
761 distribution in the northeastern Indian Ocean and their application to paleoenvironment reconstruction. *Rev. Palaeobot.*
762 *Palynol.*, 256, 50-62, doi: 10.1016/j.revpalbo.2018.05.007, 2018.

763 Luo, C., Chen, M., Xiang, R., Liu, J., Zhang, L., and Lu, J.: Comparison of modern pollen distribution between the northern
764 and southern parts of the South China Sea. *Int. J. Biometeorol.*, 59(4), 397-415, doi: 10.1007/s00484-014-0852-2, 2015.

765 Luo, C., Jiang, C., Yang, M., Chen, M., Xiang, R., Zhang, L., Liu, J., and Pan, A.: Transportation modes of pollen in surface
766 waters in the South China Sea and their environmental significance. *Rev. Palaeobot. Palynol.*, 225, 95-105, doi:
767 10.1016/j.revpalbo.2015.11.004, 2016.

768 Luo, Y., and Sun, X.: Vegetation evolution and millennial-scale climatic fluctuations since Last Glacial Maximum in pollen
769 record from northern South China Sea. *Chin. Sci. Bull.*, 50(8), 793-799, doi: 10.1007/BF03183681, 2005.

770 Luo, Y., and Sun, X.: Vegetation evolution and its response to climatic change during 3.15–0.67 Ma in deep-sea pollen record
771 from northern South China Sea. *Chin. Sci. Bull.*, 58(3), 364-372, doi: 10.1007/s11434-012-5374-x, 2013.

772 Maher, L.J.: Nomograms for computing 0.95 confidence limits of pollen data. *Rev. Palaeobot. Palynol.*, 13, 85-93, doi:
773 10.1016/0034-6667(72)90038-3, 1972.

774 Marret, F., and Zonneveld, K. A. F.: Atlas of modern organic-walled dinoflagellate cyst distribution. *Rev. Palaeobot. Palynol.*,
775 125(1–2), 1-200, doi: 10.1016/S0034-6667(02)00229-4, 2003.

776 Matsuoka, K.: Dinoflagellate cysts and pollen in pelagic sediments of the northern part of the Philippine Sea. *Bull., Faculty of*
777 *Liberal Arts, Nagasaki University. (Natural Science)*, 21(2), 59-70, 1981.

778 Meyers, P.A.: Organic geochemical proxies of paleoceanographic, paleolimnologic, and paleoclimatic processes. *Org.*
779 *Geochem.*, 27, 213-250, doi: 10.1016/S0146-6380(97)00049-1, 1997.

780 Milliman, J. D., and Syvitski, J. P. M.: Geomorphic/tectonic control of sediment discharge to the ocean: The importance of
781 small mountainous rivers. *J. Geol.*, 100(5), 525-544, doi: 10.1086/629606, 1992.

782 Mooney, S. D., and Tinner, W.: The analysis of charcoal in peat and organic sediments. *Mires Peat*, 7(09), doi:
783 10.19189/001c.128417, 2011.

784 Oppo, D. W., and Sun, Y.: Amplitude and timing of sea-surface temperature change in the northern South China Sea: Dynamic
785 link to the East Asian monsoon. *Geology*, 33(10), 785-788, doi: 10.1130/G21867.1, 2005.

786 [Sanchez Goñi, M. F., and Harrison, S. P.: Millennial-scale climate variability and vegetation changes during the Last Glacial:
787 Concepts and terminology. *Quat. Sci. Rev.*, 29\(21\), 2823-2827, doi: 10.1016/j.quascirev.2009.11.014, 2010.](#)

788 Schönfeld, J., Alve, E., Geslin, E., Jorissen, F., Korsun, S., and Spezzaferri, S.: The FOBIMO (FORaminiferal Bio-MONitoring)
789 initiative—Towards a standardised protocol for soft-bottom benthic foraminiferal monitoring studies. *Mar.*
790 *Micropaleontol.*, 94-95, 1-13, doi: 10.1016/j.marmicro.2012.06.001, 2012.

791 Smayda, T. J., and Trainer, V. L.: Dinoflagellate blooms in upwelling systems: Seeding, variability, and contrasts with diatom
792 bloom behaviour. *Prog. Oceanogr.*, 85(1), 92-107, doi: 10.1016/j.pocean.2010.02.006, 2010.

793 Stibig, H.-J., Belward, A. S., Roy, P. S., Rosalina-Wasrin, U., Agrawal, S., Joshi, P. K., Beuchle, R., Fritz, S., Mubareka, S.,
794 and Giri, C.: A land-cover map for South and Southeast Asia derived from SPOT-VEGETATION data. *J. Biogeogr.*,
795 34(4), 625-637, doi: 10.1111/j.1365-2699.2006.01637.x, 2007.

796 Stuiver, M., and Reimer, P. J.: Extended 14C Data Base and Revised CALIB 3.0 14C Age Calibration Program. *Radiocarbon*,
797 35(1), 215-230, doi: 10.1017/S0033822200013904, 1993.

798 Sun, X., Li, X., and Beug, H.-J.: Pollen distribution in hemipelagic surface sediments of the South China Sea and its relation
799 to modern vegetation distribution. *Mar. Geol.*, 156(1), 211-226, doi: 10.1016/S0025-3227(98)00180-7, 1999.

800 Sun, X., Li, X., and Chen, H.: Evidence for natural fire and climate history since 37 ka BP in the northern part of the South
801 China Sea. *Sci. China Ser. D-Earth Sci.*, 43(5), 487-493, doi: 10.1007/bf02875310, 2000a.

802 Sun, X., Li, X., Luo, Y., and Chen, X.: The vegetation and climate at the last glaciation on the emerged continental shelf of
803 the South China Sea. *Palaeogeogr., Palaeoclimatol., Palaeoecol.*, 160(3), 301-316, doi: 10.1016/S0031-0182(00)00078-
804 X, 2000b.

805 Sun, X., and Luo, Y.: Pollen record of the last 280 ka from deep sea sediments of the northern South China Sea. *Sci. China*
806 *Ser. D-Earth Sci.*, 44(10), 879-888, doi: 10.1007/BF02907079, 2001.

807 Sun, X., Luo, Y., Huang, F., Tian, J., and Wang, P.: Deep-sea pollen from the South China Sea: Pleistocene indicators of East
808 Asian monsoon. *Mar. Geol.*, 201(1), 97-118, doi: 10.1016/S0025-3227(03)00211-1, 2003.

809 Tang, L., Mao, L., Shu, J., Li, C., Shen, C., and Zhou, Z.: Atlas of Quaternary pollen and spores in China. Science Press and
810 Springer Nature Singapore Pte Ltd, doi: 10.1007/978-981-13-7103-5, 2020.

811 ter Braak, C. J. F., and Smilauer, P.: Canoco reference manual and user's guide: software for ordination, version 5.0.
812 Microcomputer Power, Ithaca, NY, USA, 2012.

813 Tian, J., Huang, E., and Pak, D. K.: East Asian winter monsoon variability over the last glacial cycle: Insights from a latitudinal
814 sea-surface temperature gradient across the South China Sea. *Palaeogeogr., Palaeoclimatol., Palaeoecol.*, 292(1-2), 319-
815 324, doi: 10.1016/j.palaeo.2010.04.005, 2010.

816 Tian, J., Wang, P. X., and Cheng, X. R.: Responses of foraminiferal isotopic variations at ODP Site 1143 in the southern South
817 China Sea to orbital forcing. *Sci. China Ser. D-Earth Sci.*, 47(10), 943-953, doi: 10.1360/03yd0129, 2004.

818 Tian, J., Xie, X., Ma, W., Jin, H., and Wang, P.: X-ray fluorescence core scanning records of chemical weathering and monsoon
819 evolution over the past 5 Myr in the southern South China Sea. *Paleoceanography*, 26(4), doi: 10.1029/2010PA002045,
820 2011.

821 Tyszkla, J., Godos, K., Goleń, J., and Radmacher, W.: Foraminiferal organic linings: Functional and phylogenetic challenges.
822 *Earth-Sci. Rev.*, 220, 103726, doi: 10.1016/j.earscirev.2021.103726, 2021.

823 Wan, S., and Jian, Z.: Deep water exchanges between the South China Sea and the Pacific since the last glacial period.
824 *Paleoceanography*, 29(12), 1162-1178, doi: 10.1002/2013PA002578, 2014.

825 Wan, S., Li, A., Clift, P. D., and Stuut, J.-B. W.: Development of the East Asian monsoon: Mineralogical and sedimentologic
826 records in the northern South China Sea since 20 Ma. *Palaeogeogr., Palaeoclimatol., Palaeoecol.*, 254(3), 561-582, doi:
827 10.1016/j.palaeo.2007.07.009, 2007.

828 Wang, C.: The forests of China. Maria Moors Cabot Foundation No.5. Harvard University, Cambridge Mass, USA, 717, 1961.

829 Wang, L., Sarnthein, M., Erlenkeuser, H., Grootes, P. M., Grimalt, J. O., Pelejero, C., and Linck, G.: Holocene variations in
830 Asian monsoon moisture: A bidecadal sediment record from the South China Sea. *Geophys. Res. Lett.*, 26(18), 2889-
831 2892, doi: 10.1029/1999GL900443, 1999.

832 Wang, P., Li, Q., and Tian, J.: Pleistocene paleoceanography of the South China Sea: Progress over the past 20years. *Mar.*
833 *Geol.*, 352, 381-396, doi: 10.1016/j.margeo.2014.03.003, 2014.

834 Wang, P., and Sun, X.: Last glacial maximum in China: comparison between land and sea. *Catena*, 23(3), 341-353, doi:
835 10.1016/0341-8162(94)90077-9, 1994.

836 Wang, P., Wang, B., Cheng, H., Fasullo, J., Guo, Z., Kiefer, T., and Liu, Z.: The global monsoon across time scales:
837 Mechanisms and outstanding issues. *Earth-Sci. Rev.*, 174, 84-121, doi: 10.1016/j.earscirev.2017.07.006, 2017.

838 Wang, X., Sun, X., Wang, P., and Stattegger, K.: Vegetation on the Sunda Shelf, South China Sea, during the Last Glacial
839 Maximum. *Palaeogeogr., Palaeoclimatol., Palaeoecol.*, 278(1), 88-97, doi: 10.1016/j.palaeo.2009.04.008, 2009.

840 Wang, Y. J., Cheng, H., Edwards, R. L., An, Z. S., Wu, J. Y., Shen, C.-C., and Dorale, J. A.: A high-resolution absolute-dated
841 late Pleistocene monsoon record from Hulu Cave, China. *Science*, 294(5550), 2345-2348, doi: 10.1126/science.1064618,
842 2001.

843 Wei, G., Liu, Y., Li, X., Shao, L., and Fang, D.: Major and trace element variations of the sediments at ODP Site 1144, South
844 China Sea, during the last 230 ka and their paleoclimate implications. *Palaeogeogr., Palaeoclimatol., Palaeoecol.*, 212(3),
845 331-342, doi: 10.1016/j.palaeo.2004.06.011, 2004.

846 Whitmore, T. C.: Rain forests: Tropical rain forests of the far east. *Science*, 228(4701), 874-875, doi:
847 10.1126/science.228.4701.874, 1985.

848 Williams, G., Fensome, R., and MacRae, R.: DINOFLAJ3, 2017.

849 Xie, S.-P., Deser, C., Vecchi, G. A., Ma, J., Teng, H., and Wittenberg, A. T.: Global Warming Pattern Formation: Sea Surface
850 Temperature and Rainfall. *J. Clim.*, 23(4), 966-986, doi: 10.1175/2009JCLI3329.1, 2010.

851 Xie, X., Zheng, H.-B., and Qiao, P.-J.: Millennial climate changes since MIS 3 revealed by element records in deep-sea
852 sediments from northern South China Sea. *Chin. Sci. Bull.*, 59(8), 776-784, doi: 10.1007/s11434-014-0117-9, 2014.

853 Xu, D., Lu, H., Wu, N., Liu, Z., Li, T., Shen, C., and Wang, L.: Asynchronous marine-terrestrial signals of the last deglacial
854 warming in East Asia associated with low- and high-latitude climate changes. *Proc. Natl. Acad. Sci. USA*, 110, 9657 -
855 9662, 10.1073/pnas.1300025110, 2013. Yu, S., Zheng, Z., Chen, F., Jing, X., Kershaw, P., Moss, P., Peng, X., Zhang, X.,
856 Chen, C., Zhou, Y., Huang, K., and Gan, H.: A last glacial and deglacial pollen record from the northern South China
857 Sea: New insight into coastal-shelf paleoenvironment. *Quat. Sci. Rev.*, 157, 114-128, doi:
858 10.1016/j.quascirev.2016.12.012, 2017.

859 Yuan, Y. C., Bu, X. W., Liao, G. H., Lou, R. Y., Su, J. L., and Wang, K. S.: Diagnostic calculation of the upper-layer circulation
860 in the South China Sea during the winter of 1998. *Acta Oceanol. Sin.*, 23(2), 187-199, 2004.

861 [Zanzarini, V., Andersen, A. N., and Fidelis, A.: Flammability in tropical savannas: Variation among growth forms and seasons](#)
862 [in Cerrado. *Biotropica*, 54\(4\), 979-987, doi: 10.1111/btp.13121, 2022.](#)

863 Zhang, H., Liu, C., Jin, X., Shi, J., Zhao, S., and Jian, Z.: Dynamics of primary productivity in the northern South China Sea
864 over the past 24,000 years. *Geochem. Geophys. Geosyst.*, 17(12), 4878-4891, doi: 10.1002/2016GC006602, 2016.

865 Zhao, X., Dupont, L., Schefuß, E., Bouimetarhan, I., and Wefer, G.: Palynological evidence for Holocene climatic and
866 oceanographic changes off western South Africa. *Quat. Sci. Rev.*, 165, 88-101, doi: 10.1016/j.quascirev.2017.04.022,
867 2017.

868 Zheng, Z., and Lei, Z. Q.: A 400,000 year record of vegetational and climatic changes from a volcanic basin, Leizhou Peninsula,
869 southern China. *Palaeogeogr., Palaeoclimatol., Palaeoecol.*, 145(4), 339-362, doi: 10.1016/S0031-0182(98)00107-2,
870 1999.

871 Zhong, Y., Chen, Z., Li, L., Liu, J., Li, G., Zheng, X., Wang, S., and Mo, A.: Bottom water hydrodynamic provinces and
872 transport patterns of the northern South China Sea: Evidence from grain size of the terrigenous sediments. *Cont. Shelf*
873 *Res.*, 140, 11-26, doi: 10.1016/j.csr.2017.01.023, 2017.

874 Zhou, B., Zheng, H., Yang, W., Taylor, D., Lu, Y., Wei, G., Li, L., and Wang, H.: Climate and vegetation variations since the
875 LGM recorded by biomarkers from a sediment core in the northern South China Sea. *J. Quat. Sci.*, 27(9), 948-955, doi:
876 10.1002/jqs.2588, 2012.

877 Zonneveld, K. A. F., Harper, K., Klügel, A., Chen, L., De Lange, G., and Versteegh, G. J. M.: Climate change, society, and
878 pandemic disease in Roman Italy between 200 BCE and 600 CE. *Sci. Adv.*, 10(4), eadk1033, doi: 10.1126/sciadv.adk1033,
879 2024.

880 Zonneveld, K. A. F., Marret, F., Versteegh, G. J. M., Bogus, K., Bonnet, S., Bouimetarhan, I., Crouch, E., de Vernal, A.,
881 Elshanawany, R., Edwards, L., Esper, O., Forke, S., Grosfjeld, K., Henry, M., Holzwarth, U., Kieft, J. F., Kim, S.,
882 Ladouceur, S., Ledu, D., Chen, L., Limoges, A., Londeix, L., Lu, S. H., Mahmoud, M. S., Marino, G., Matsouka, K.,
883 Matthiessen, J., Mildenhall, D. C., Mudie, P., Neil, H. L., Pospelova, V., Qi, Y., Radi, T., Richerol, T., Rochon, A.,
884 Sangiorgi, F., Solignac, S., Turon, J. L., Verleye, T., Wang, Y., Wang, Z., and Young, M.: Atlas of modern dinoflagellate
885 cyst distribution based on 2405 data points. *Rev. Palaeobot. Palynol.*, 191(0), 1-197, doi: 10.1016/j.revpalbo.2012.08.003,
886 2013.

887 Zonneveld, K. A. F., and Pospelova, V.: A determination key for modern dinoflagellate cysts. *Palynology*, 39(3), 387-409, doi:
888 10.1080/01916122.2014.990115, 2015.

889 Zonneveld, K. A. F., Versteegh, G., and Kodrans-Nsiah, M.: Preservation and organic chemistry of Late Cenozoic organic-
890 walled dinoflagellate cysts: A review. *Mar. Micropaleontol.*, 68(1-2), 179-197, doi: 10.1016/j.marmicro.2008.01.015,
891 2008.